DISSERTATIONES
PHYSICAE
UNIVERSITATIS
TARTUENSIS
112

MIKK ANTSOV

Tribomechanical properties of individual 1D nanostructures: experimental measurements supported by finite element method simulations

DISSERTATIONES PHYSICAE UNIVERSITATIS TARTUENSIS
112

DISSERTATIONES PHYSICAE UNIVERSITATIS TARTUENSIS
112

MIKK ANTSOV

Tribomechanical properties of individual 1D nanostructures: experimental measurements supported by finite element method simulations

UNIVERSITY OF TARTU
Press

Institute of Physics, University of Tartu

The dissertation was admitted on 27.06.2017 in partial fulfilment of the requirements for the degree of Doctor of Philosophy in Physics, and was allowed for defence by the Council of the Institute of Physics, University of Tartu.

Supervisors: Dr. Sergei Vlassov, Institute of Physics, University of Tartu

Dr. Leonid Dorogin, Peter Grünberg Institute and Institute for Advanced Simulation, Jülich Forschungszentrum

Dr. Rünno Lõhmus, Institute of Physics, University of Tartu

Opponents: Dr. Dirk Dietzel, Justus-Liebig-Universität Gießen

Dr. Valdek Mikli, Tallinn University of Technology

Defense: August 29, 2017, at the University of Tartu, Tartu; Estonia

This work has been partially supported by Graduate School of Functional materials and technologies receiving funding from the European Regional Development Fund in University of Tartu, Estonia

ISSN 1406-0647
ISBN 978-9949-77-519-4 (print)
ISBN 978-9949-77-520-0 (pdf)

University of Tartu Press
www.tyk.ee

CONTENTS

LIST OF ORIGINAL PUBLICATIONS

1) **Antsov, Mikk**; Dorogin, Leonid; Vlassov, Sergei; Polyakov, Boris; Vahtrus, Mikk; Mougin, Karine; Lõhmus, Rünno; Kink, Ilmar (2014). Analysis of static friction and elastic forces in a nanowire bent on a flat surface: a comparative study. Tribology International, 72, 31–34, 10.1016/j.triboint.2013.12.010.

2) Vlassov, S.; Polyakov, B.; Dorogin, L.; Vahtrus, M.; Mets, M.; **Antsov, M.**; Saar, R.; Romanov, A.; Lõhmus, A.; Lõhmus, R. (2014). Shape restoration effect in Ag-SiO_2 core-shell nanowires. Nano Letters, 14 (9), 5201–5205, 10.1021/nl5019063.

3) Polyakov, Boris; Vlassov, Sergei; Dorogin, Leonid; Novoselska, Natalia; Butikova, Jelena; **Antsov, Mikk**; Oras, Sven; Lõhmus, Rünno; Kink, Ilmar (2014). Some aspects of formation and tribological properties of silver nanodumbbells. Nanoscale Research Letters, 9, Article 186, 10.1186/1556-276X-9-186.

4) Vlassov, Sergei; Polyakov, Boris; Oras, Sven; Vahtrus, Mikk; **Antsov, Mikk**; Šutka, Andris; Smits, Krisjanis; Dorogin, Leonid; Lõhmus, Rünno (2016). Complex tribomechanical characterization of ZnO nanowires: nanomanipulations supported by FEM simulations. Nanotechnology, 27 (33), 335701, 10.1088/0957-4484/27/33/335701.

5) Polyakov, Boris; **Antsov, Mikk**; Vlassov, Sergei; Dorogin, Leonid; Vahtrus, Mikk; Zabels, Roberts; Lange, Sven; Lõhmus, Rünno (2014). Mechanical properties of sol-gel derived SiO_2 nanotubes. Beilstein Journal of Nanotechnology, 5, 1808–1814

Ready for submission:

6) Antsov, Mikk; Dorogin, Leonid; Polyakov, Boris; Mets, Magnus; Oras, Sven; Vahtrus, Mikk; Lõhmus, Rünno; Vlassov, Sergei; Comparative analysis of mechanical test configurations for gold nanowires and nanoplates

Author's contribution:

Paper 1: Author is responsible for elaboration of the new model, calculations and preparation of the manuscript.

Papers 2–4: Author is responsible for all FEM simulations.

Paper 5–6: Author is responsible for all FEM simulations and AFM and SEM measurements.

PUBLICATIONS NOT INCLUDED IN THESIS

1) Polyakov, B.; Dorogin, L.; Vlassov, S.; **Antsov, M**.; Kulis, P.; Kink, I.; Lõhmus, R. (2012). In situ measurements of ultimate bending strength of CuO and ZnO nanowires. The European Physical Journal B – Condensed Matter and Complex Systems, 85 (11), Article 366, 10.1140/epjb/e2012-30430-6.

2) Dorogin, L.; Vlassov, S.; Polyakov, B.; **Antsov, M**.; Lõhmus, R.; Kink, I.; Romanov, A. (2013). Real-time manipulation of ZnO nanowires on a flat surface employed for tribological measurements: experimental methods and modelling. physica status solidi (b), 250 (2), 305–317, 10.1002/pssb.201248445.

3) Polyakov, B.; Vlassov, S.; Dorogin, L.; Butikova, J.; **Antsov, M**.; Oras, S.; Lõhmus, R.; Kink, I.. (2014). Manipulation of nanoparticles of different shapes inside a scanning electron microscope. Beilstein Journal of Nanotechnology, 5, 133–140,

4) Vlassov, S.; Polyakov, B.; Dorogin, L.; **Antsov, M**.; Mets, M.; Umalas, M.; Saar, R.; Lõhmus, R.; Kink, I. (2014). Elasticity and yield strength of pentagonal silver nanowires: In situ bending tests. Materials Chemistry and Physics, 143 (3), 1026–1031, j.matchemphys.2013.10.042.

5) Polyakov, B.; Vlassov, S.; Dorogin, L.; Butikova, J.; Smits, K.; **Antsov, M**.; Oras, S.; Zabels, R.; Lõhmus, R. (2015). Metal nanodumbbells for nanomanipulations and tribological experiments. Physica Scripta, 90 (9), 094007, 0031-8949/90/9/094007.

6) Klaas, M.; Kangur, T.; Viil, J.; Mäemets-Allas, K.; Minajeva, A.; Vadi, K.; **Antsov, M**.; Lapidus, N.; Järvekülg, M.; Jaks, V. (2016). The alterations in the extracellular matrix composition guide the repair of damaged liver tissue. Scientific Reports, 6, 10.1038/srep27398.

7) Mets, M.; **Antsov, M**.; Zadin, V.; Dorogin, L.; Aabloo, A.; Polyakov, B.; Lõhmus, R.; Vlassov, S. (2016). Structural factor in bending testing of fivefold twinned nanowires revealed by finite element analysis. Physica Scripta, 91 (11), 115701 (7pp)

8) Vahtrus, M.; Šutka, A.; Polyakov, B.; Oras, S.; **Antsov, M**.: Doebelin, N.; Lõhmus, R.; Nõmmiste, E.; Vlassov, S.; (2016). Effect of cobalt doping on the mechanical properties of ZnO nanowires. Materials Characterization, 121, 40–47, 10.1016/j.matchar.2016.09.027.

9) Šutka, A.; **Antsov, M**.; Järvekülg, M.; Visnapuu, M.; Heinmaa, I.; Mäeorg, U.; Vlassov, S.; Šutka, A. (2017). Mechanical properties of individual fiber segments of electrospun lignocellulose-reinforced poly(vinyl alcohol). Journal of Applied Polymer Science, 134 (2), 44361, 10.1002/app.44361.

10) Taaber, T.; **Antsov, M**.; Vlassov, S.; Mäeorg, U.; Dorogin, L.; Järvekülg, M.; Saal, K.; Lõhmus, R. (2017). Formation and characterization of microcantilevers produced from ionic liquid by electron beam irradiation. Journal of Molecular Liquids, 229, 45–50, 10.1016/j.molliq.2016.12.034.

11) Joost, U.; Šutka, A.; Visnapuu, M.; Tamm, A.; Lembinen, M.; **Antsov, M**.; Utt, K.; Smits, K.; Nõmmiste, E.; Kisand, V.; (2017). Colorimetric gas detection by the varying thickness of a thin film of ultrasmall PTSA-coated TiO2 nanoparticles on a Si substrate. Beilstein Journal of Nanotechnology, 8, 229–236, 10.3762/bjnano.8.25.

ABBREVIATIONS

1D	One dimensional
NW	Nanowire
1DNS	One dimensional nanostructure
FEM	Finite element method
NEMS	Nanoelectromechanical system
AFM	Atomic force microscope
3D	Three dimensional
LED	Light emitting diode
QTF	Quartz tuning fork
QMB	Quartz Microbalance
SEM	Scanning electron microscope
3PB	Three point bending
MD	Molecular dynamics
FM	Frequency modulation
AM	Amplitude modulation
VTM	Vapour transport method
NT	Nanotube
HRSEM	High resolution scanning electron microscope
TEM	Transmission electron microscope
NP	Nanoplate
DB	Dumb-bell
ND	Nanodumb-bell
A	Hamaker constant

PREFACE

The thesis belongs to the field of nanotechnology and is dedicated to investigation of mechanical and tribological properties of 1D nanostructures (1DNS) by advanced experimental techniques supported by finite element method (FEM) simulations and analytical calculations.

1DNS such as nanowires, nanotubes, nanofibers etc. are among the most important materials in modern science and have number of promising applications including nanowaveguides, sensors, nanoelectromechanical systems (NEMS) based on a single 1DNS and many others. Applications often involve deformation and movement of the 1DNS, therefore understanding of mechanics and tribology of such systems is essential for reliable operation of 1DNS-based devices. It is known that properties of the nanoscale materials are often superior in comparison to their bulk counterparts. At the same time situation is complicated by the fact that those properties depend on the size and geometry of the nanostructures. Moreover, there are number of serious challenges related to the characterization and manipulation of the nanoscale objects.

The ultimate goal of the present study is the development of the appropriate experimental methods and corresponding models for advanced characterization of mechanical and tribological properties of individual 1DNS.

Experimental characterizations of 1DNS covered in this thesis are based on the *in situ* nanomanipulaton technique inside a scanning electron microscope as well as the atomic force microscope based measurements. All experiments are strongly supported by analytical calculations and FEM simulations for revealing physical phenomena, which otherwise would be difficult to obtain analytically.

The thesis is divided into 5 chapters. In the first chapter, a brief introduction to the mechanical characterization of individual 1DNS is given. A number of expected benefits of 1D nanostructures are discussed as well as the problems and challenges related to the study and applications of such structures. The cantilevered bending, 3PB and nanoindentation techniques are discussed and their applicability in the nanoscale is revealed. In the second part the tribological behavior of 1DNS is discussed and a number of methods for studying the frictional behavior are shown. The third part deals with the applicability of the finite element method for the analysis of the mechanical and tribological behavior of 1DNS. The forth part, consisting of obtained results and discussion, can be divided into three subsections. Two of those are related to the experimental measurements conducted with the AFM (atomic force microscope) and *in situ* nanomanipulation technique. The third subsection covers all the FEM simulations related to the experiments performed in the two subsections.

1. INTRODUCTION

1.1. One-dimensional nanostructures

It is known that properties of nanoscale materials can be very different in comparison to their 3D counterparts [1]. Moreover, those properties often depend of size and geometry of the nanostructures. This is conditioned by the several factors including high surface-to-volume ratio and quantum confinement effects. The first reason (surface effect) is related to the fact that atoms of a few outer layers have different properties (higher free energy, higher packing density, increased stiffness etc) in comparison to bulk atoms. The smaller the structure the higher is the contribution of surface atoms in its properties. The second (quantum) effect arises when dimensions of the structure become comparable with the length scale of different physical phenomena such as electron free path, phonon free path, Bohr exciton radius etc. Important advantage of nanostructures is that some of the materials parameters, like e.g. stiffness or thermal conductivity, can be independently controlled and even nanostructures made of the same material may possess dissimilar properties due to differences in their crystal phase, crystalline size, surface conditions, and aspect ratios.

Modern chemical and physical synthesis techniques provide great control over the size, shape and composition of nanostructures allowing to produce structures with high aspect ratio – so called one-dimensional nanostructures like nanowires, nanotubes, nanofibers etc. Being nanoscale in two dimensions 1DNS have most of the beneficial properties nanostructures in general including increased surface area, enhanced exciton binding energy, diameter-dependent band gap, increased surface scattering for electrons and phonons, and other peculiarities [2]. At the same time the length of such structures can achieve even few millimeters [3]making them unique class of materials that bridge nanoscopic and macroscopic scales. For instance, in contrast to other low dimensional systems, 1DNS have two quantum confined directions, while still leaving one unconfined direction for electrical conduction, allowing applications where electrical conduction, rather than tunneling transport, is required.

1DNS can be made from a wide range of materials, and can be metallic, semiconducting or insulating. Due to unique characteristics 1DNS have number of promising applications including interconnects in nanoelectronics, waveguides in nanophotonics and plasmonics, nanorelays and nanoswitches, nanosensors, nanogenerators etc [4].

The before mentioned can give rise to a number of interesting mechanical, chemical, elecromagnetical and optical properties of 1DNS which differ from the same material properties of bulk structures. These properties and small size are one of the reasons, why 1DNS have a huge potential in different applications and mechanisms, including field effect transistors, light emitting diodes, nanolasers, solar cells, chemical and biological sensors etc.

Even more interesting properties can be obtained by combining different materials in a single 1D core/shell type heterostructure. In comparison to homo-

genious nanomaterials, heterostructures not only have richer chemical compositions and morphologies, but also may display strongly improved functionalities and can be tailored to meet complex technological needs in electronics, photonics, catalysis, sensing, optoelectronics, electrochemical, and mechanical devices. E.g. coating can strongly enhance optical properties of metallic NWs enabling applications in high-efficiency solar cells and realization of LED devices based on single 1DNS [5,6,7].

1.2. Mechanical characterization of 1D nanostructures

In numerous applications 1DNS are subjected to mechanical stresses. E.g. in flexible electrodes, as well as in various nanoelectromechanical systems (NEMS) like nanorelays, nanoswitches [8] and nanoresonators [9], 1DNS should withstand numerous repetitive deformations. In nanophotonics large bending deformations of nanofiber is often required to guide the light in desired direction. Defects or discontinuities such as cracks introduced by bending affect surface plasmon resonance and light propagation in waveguides [10,11]. As many other properties, mechanical properties of 1DNS can differ drastically from macroscopic analogs. Starting from exceptional strength [12] to more exotic phenomena like unexpected plasticity of covalent materials at the nanoscale [13]. Mechanical properties of 1DNS can be modified further by coating with different materials. Theoretical studies predicted number of interesting effects on mechanical properties due to composite structure. For example, Aifantis demonstrated that the presence of the interface between the core and the shell influences significantly the overall plastic response of a NW during loading [14]. Liu et al found nonlinear dependence of Young modulus on composition and attributed effect to the different components and the different strains in the interfaces between the cores and the shells. [15]. However, explanation of some observed effects could not be directly derived from available theoretical models. Therefore, a deeper understanding and control over elasticity, plasticity, fatigue and fracture of 1DNS, as well as further elaboration of existing models, is essential for performance and reliability of devices based on 1DNS.

Manipulation and characterization of individual nanostructures is not a trivial task. The small size of nanostructures give raise to serious challenges related to probing of their properties. High aspect ratio of 1DNS facilitates manipulation of such structures and gives more flexibility in conduction of experiments with individual objects in comparison to nanoparticles (0D) or nanofilms (2D). Therefore, 1DNS are attractive not only from the viewpoint of applications, but also as more convenient test objects for investigation of the nanoscale phenomena.

There are number of different techniques have been proposed and applied for mechanical characterization of 1DNS. The most common include three-point bending (3PB), tensile test, cantilever beam bending and nanoindentation technique. Short description of the listed methods is provided below.

1.2.1. Nanoindentation

The nanoindentation experiment consists of primarily six different components, which are paramount in conduction a proper indentation test. The test material, the precise sensors and actuators used for applying and measuring the mechanical response of the material and both the indenter displacement and the geometry of the indenter tip are the most critical components of the indentation system. Typically the indentation tip is made out of diamond, which has really sharp geometry, is symmetric and without defects. Also other tips may be used, but the choice of tip depends on the studied material. A nanoindentation experiments consists of two stages, the tip is approached to the surface and then again retracted. During this procedure, the indentation tip is pressed against the studied material and as a result, an upward force acts on the tip. The displacement of the tip can be converted into force, so as a result, a force-displacement curve is obtained. The force-displacement curve for different materials typically varies. This is due to the variation of the mechanical properties of the studied materials. [16] The nanoindentation test can be used for studying the plasticity of nanostructures [17], the measurement of the elastic modulus of thin films [18] and even the viscous properties of materials [19].

1.2.2. Cantilevered beam bending technique

The cantilevered beam bending technique is based on the bending of a prismatic beam from one end, while the other end is fixed. There are number factors that should be considered for efficient application of the technique. The most critical of them is the proper knowledge of the geometrical parameters of the beam. As we are dealing with beams in the nanoscale, the precision of the measurement of the geometric properties is crucial. Even a slight error can affect the overall accuracy of the method. Secondly, the clamping of the structure must be sufficient for being able to bear loads in the order of hundreds of nN up to several μN. Thirdly, the point of application of the external force must be controlled with high accuracy, so the need for high precision nanomanipulators is a necessity. The cantilevered beam bending technique has been used for studying mechanical properties of different 1DNS. Gordon et al. [20] measured the elastic modulus and fracture strength of as-grown Si [111] NWs with an AFM based multi-point cantilevered beam bending technique. He was able to reveal an increase of the Young's modulus and fracture strength with decreasing diameter of the NWs. The fracture strength of ZnO NWs was shown to increase by 2–3 orders of magnitude (from MPa to GPa). Polyakov et al. Manoharan et al [21] studied the elastic modulus of vapor-liquid-solid grown ZnO NWs. An AFM cantilever was used for bending the cantilevered NW and taking SEM micrographs during the bending experiment, both the deflection of the AFM cantilever and the NW can be visualized. Knowing the stiffness of the AFM cantilever, one is able to calculate the force acting on the NW and using the elastic beam theory is able to calculate the Young's modulus. The measured

values of Young's moduli ranged from 35 GPa to 44 GPa, for NWs with diameters in the range of 350–750 nm.

1.2.3. Three point bending technique

A typical 3PB experimental setup consists of a prismatic rod being deflected from the middle point while lying over a trench or a hole on the substrate. The studied beam can be either free or fixed from the sides, depending on the experimental configuration. During the deflection of the middle point, the corresponding force is registered with a force sensor. In the AFM based configuration the sensing element is the AFM cantilever, which is used also for imaging of the prismatic rod. The experimental configuration is quite versatile, but one should always consider the studied materials. If for example, the studied structure is larger and stiffer than the used cantilever, one will only measure the deformation of the cantilever and AFM tip and as a result, no information about the studied structure can be gained. Also, the hardness of the cantilever must be larger than the studied material, otherwise a similar effect will happen as mentioned before. But if all parameters are chosen correctly, one is able to perform 3PB experiments on nanomaterials. Such technique was used by Zhang et al. [22], who measured the Young's modulus of LaB_6 NWs. He was able to show, that the measured elastic modulus of single crystal LaB_6 was larger than the sintered polycrystalline LaB_6. He also measured the hardness of the NWs and showed that it was higher than single crystal LaB_6 and tungsten metals. In a related work using the AFM based 3PB technique, Corrales et al. [23] characterized sintered silica fibers with and without voids of sizes 60 nm or 260 nm. He showed that voids can be used as means to control the mechanical stiffness and fracture properties of the studied silica fibers. The breaking of the fibers was related to the cavitation.

1.2.4. Tensile test

The tensile test is one of the most used methods for measuring the mechanical properties of many macroscopic materials. The typical setup consists of a prismatic rod, which is fixed from both ends and an axial load is applied to induce deformation. The resulting force-deflection curve can be used for describing the mechanical response of the studied material. The Young's modulus as well as the plastic yield values can be measured with the technique. The method has also been shown to be applicable in measuring the mechanical properties of individual nanostructures. Xu. et al. [24] performed the tensile test on ZnO NWs clamped between a AFM cantilever and a tip attached to a nanomanipulator. He was able to measure the elastic modulus of seven NWs having diameters from 20 nm to 80 nm. The obtained Young's modulus values were in range of 140 GPa to 170 GPa and was able to show, that the elastic modulus is size dependent. In another work conducted by Fu. et al [25], he

manipulated carbon nanotubes clamped between two AFM tips in SEM with a nanomanipulator and was able to show, that it is possible to induce bending, kinking and breaking of nanotubes.

1.2.5. Peculiarities of nanomechanical characterization

As the forces due to the small size of the nanostructures is in the range of a few nN to uN, the standard methods applied typically in the mechanical testing of engineering materials are not applicable, as they do not possess the required sensitivity. As a consequence, extremely fine measurement techniques and sensors must be applied. The most common approach to nanomechanical characterization is based on atomic force microscope (AFM), where a small cantilever deformation can be detected by means of an optical feedback system. The AFM tip itself can act as one of such force sensors. Other means involve the electromechanical devices such as the QTF (quartz tuning fork), where the mechanical response is determined by means of the change in the oscillating parameters of the system.

Visualization of the measured 1DNS can be accomplished by means of applying different microscopy techniques. Nanostructures of interest can be visualized by AFM. However, AFM have disadvantage of being unable to perform measurements and obtain image at the same time, which means, that the behavior of 1DNS under deformation and events like e.g. crack formation and propagation cannot be observed in real time. The image can be taken only before and after the mechanical testing. It also makes AFM-based techniques time-consuming. However, due to high precision and accuracy AFM is still the most common tool for nanomechanical characterization of 1DNS.

Some of the shortcomings of the AFM can be overcome by combining it with scanning or transmission electron microscopes (SEM and TEM). This is realized by equipping an electron microscope with a nanopositioner and force sensor. Such *in situ* nanomanipulation and measurements techniques enable fast and real time visualization of the measurement procedure. However, there are also certain shortcomings related to the use of e-beam radiation. Firstly, the studied 1DNS are being constantly bombarded by electrons, which might affect the studied objects by damaging or changing the structure. Secondly, for longer exposure times or in the presence of hydrocarbons the structure of interest can be contaminated by e-beam induced carbon deposition. Moreover, *in situ* techniques are suitable only for conductive or semiconducting materials to avoid charging induced by incident beam.

It should be noted that the interpretation of the results is another difficult task in measuring and characterizing 1DNS. In the nanoscale, there are a number of factors, which might influence the correct interpretation of the measurements. For example, when the studied 1DNS are too thin, than the surface under the nanostructure can affect the measurement directly by seemingly making the material stiffer. This is called the “anvil effect.” and it has been noticed in the

measurements of thin films etc. [26]. Additionally in nanoindentation and 3PB experiments, the deformation of the AFM tip is not taken into account, as it is assumed, that the stiffness of the tip is higher, than that of the studied materials. There are also number of technical aspects and human factors that increase the scattering and uncertainty of the results.

1.3. Tribological characterization of 1D nanostructures

In addition to mechanical properties, another crucial parameter for the manipulation and assembly of 1DNS-based system is the friction between 1DNS and substrate.

Friction is one of the oldest and most important subjects both from practical and fundamental points of view. The main laws of friction were formulated already by da Vinci and Amonton. Since then we know, that friction is proportional to normal load and is independent of apparent contact area. However in recent years it was found that for description of nanoscale systems classical laws of friction cannot be applied. [27] One of the reasons is related to real contact area. When two macroscopic bodies are brought into contact they will contact only in the place of certain asperities, and real contact area will be many orders of magnitude smaller than apparent. If external load is applied pushing bodies towards each other, then contacting asperities will deform and real contact area will increase. Therefore actually friction is directly related to the contact area. For the nanoscale system the size of the objects is comparable or even smaller than the size of a single asperity, so that we can have systems where apparent and real contact areas can be the same or very similar. Gravity and inertia are negligible at such scales and surface forces dominate. Therefore, tribological behavior of single nanostructures will be very different from our everyday experience. Examples include, but not limited to huge difference between static and kinetic friction, dependence of friction on time in contact, temperature, applied electric potential, on direction of motion, absence of friction for in-commensurate systems, etc.

1DNS is one of the most convenient test objects to study the nanoscale friction as it can be used without external force sensors. The system consists of 1DNS on top of a flat substrate and a nanomanipulator. When 1DNS is dragged on the surface in its midpoint it bends into an arc. The radius of curvature is determined by the interplay between elastic restoration forces in 1DNS and 1DNS/substrate friction. If stiffness of the 1DNS in known, then friction can be easily extracted from the profile of the 1DNS. Such approach, however, requires visual guidance to register the profile of 1DNS during manipulation.

Different physical properties can be studied by such a setup like adhesion and friction between NW and surface. Despite the simple approach, this setup can relate to many realistic applications. Several studies of such a configuration with a variety of NWs have been performed in the last decades.

For example, Roy, et al. [28] applied the visually guided nanomanipulation method for studying the kinetic friction between ZnO NWs and surfaces of SiO_2 and SiN. He showed that the difference in frictional stress might be caused by the different Hamaker constants of the materials and the varying surface roughness of the substrate.

In another study, the static friction force between a silicon NW and elastomeric substrates were measured by Qin et al. [29] He was able to use the most bent state of a NW lying on the flat substrate and show, that if the elastomeric substrate (poly-dimetylsiloxane (PDMS)) is treated by ultraviolet radiation and ozone, an initial increase in static friction is directly followed by an decrease. The time-dependent effect was due to the hydrophobic recovery of PDMS surface.

1.4. Finite element method simulations for mechanical and tribological characterization of 1D nanostructures

In the last few decades the focus from the theoretical and experimental physics has moved a lot further to the computational and simulation based physics. This is largely due to the rise of the computational power of computers and the amount of advanced modeling methods developed for different physical problems. Those methods include such as Ab-Initio [30], Discrete Dislocation Dynamics [31], Finite Element Method (FEM) [32,33] and Molecular Dynamics [34,35,36]. Most of them can be used for simulating both the mechanical and tribological problems of different materials and interfaces. The most classical techniques of those are the MD (molecular dynamics) [37] and FEM methods [38,39]. The MD approach is an atomistic approach, where atomic nuclei are represented as point masses and classical Newtonian mechanics are used for the interaction between the nuclei. [40,41] As real nanoscale contacts and objects consist of a huge number of atoms, the computational power required for solving the Newtonian equations and the time consumed are also large. So for simulating nanoscale interactions, MD is not the best method. Alternatively, FEM has shown to be relatively fast and comprehensive method for simulating mechanical properties and interfacial effects at the nanoscale. Using the purely continuum or atomistic simulations have shown a number of difficulties, as they cannot be completely linked to the realistic experiments. But they are able to give some insight into the studied problems.

The finite element method is a numerical analysis technique designed to obtain an approximate solution to any number of partial differential equations governing the laws of physics for space- and time-dependent problems. For many such problems, the partial differential equations cannot be solved by analytical methods and instead, the equations can be generated so, that they are based on several types of discretization. The methods enable one to approximate the partial differential equations with numerical equations, which give an approximate solution to the partial differential equations. Typically the studied

problem is divided into small elements for which a set of equations is defined and solved numerically. Several solver algorithms can also be applied for obtaining a solution, which depends on the set problem, direct or iterative.

Several FEM based studies for simulating the mechanical response of nanostructures have been conducted in the last decade. For example, Yvonett et al [42] studied the size-dependent mechanical properties of nanowires by FEM taking into consideration the free surface effects. He was able to show, that both FEM and ab-initio method gave relatively comparable results for the size dependence of Young's modulus and for the residual axial and radial strain. The method was also applied for calculating the stiffness of a NW in complex bending configuration and a direct dependence on the diameter of the NW was shown. A novel μLaue diffraction based method in combination with FEM modeling was conducted by Leclere et al. [43], who studied single-crystalline Au NWs by AFM based 3PB technique. During the bending test, the μLaue diffraction patterns were recorded and the bending angle was measured. The experimental bending was compared to a FEM simulation, which revealed stresses present in the NW twice as high as the elastic limit of Au. These are just some of the experiments conducted on NWs, where FEM is used for revealing internal stresses and mechanical properties of nanostructures.

FEM has also been applied for characterizing different tribological phenomenon both in the micro-[44] and nanoscale [45]. Xie et al.[46] employed FEM simulations for the analysis of non-uniform distribution of kinetic friction between Al_2O_3 NWs and silicon having a number of complex surface textures. As a result, the friction force per unit effective contact length could be calculated and it was shown, that friction force per unit length is proportional to the effective contact area between NW and substrate.

2. AIMS OF THE STUDY

The ultimate goal of the present study consist in the development of the appropriate experimental methods and corresponding models for advanced characterization of mechanical and tribological properties of individual 1D nanostructures. To achieve this goal a number of objectives were set, which consist of both experimental and theoretical parts. Main objectives are listed below.

- To elaborate more realistic analytical and FEM-based models of stress distribution between elastically bent 1DNW and flat substrate.
- To create FEM model of composite core-shell NW consisting of elastic core and viscous shell for simulation of its behavior in bending test.
- To find appropriate experimental method and appropriate FEM model for mechanical characterization of tubular 1DNS with thick walls.

3. RESULTS AND DISCUSSION

3.1. *In situ* nanomanipulation experiments inside scanning electron microscope for mechanical characterization of 1D nanostructures

3.1.1. Experimental setup

All experiments were conducted inside a scanning electron microscope (SEM, (Tescan VEGA II SPU and FEI Helios Nanolab 600)) via the *in situ* nanomanipulation (Smaract nanomanipulator, Kleindiek micromanipulator) method or with an atomic force microscope (AFM) (Bruker Dimension Edge). The nanomanipulation setup can be seen in Figure 1.

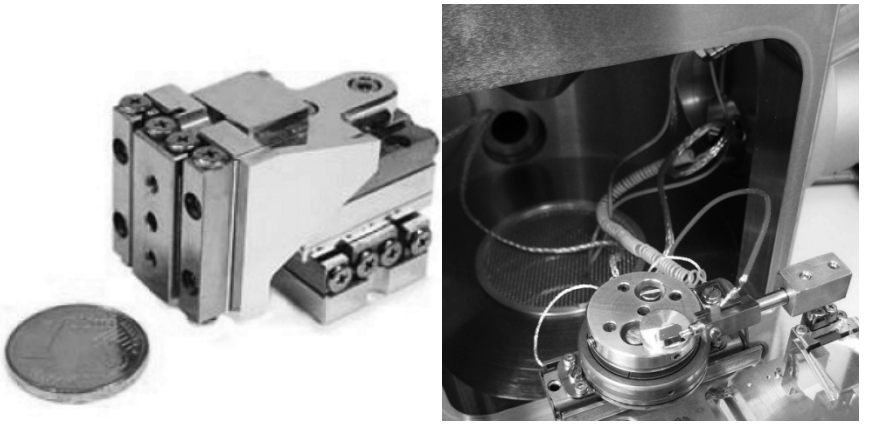

Figure 1. (left) SmarAct nanomanipulator. (right) Nanomanipulator with QTF force sensor inside SEM.

Most of the cantilevered bending experiments were conducted inside SEM and all the 3PB and nanoindentation experiments were conducted using the AFM. The forces in the cantilevered beam bending experiments were measured by a homemade force sensor. The sensor consisted of a quartz tuning fork (QTF) with a sharp tip glued to one prong. The same configuration has been used as a sensitive element in scanning probe microscopy to control the gap between the sharp tip and the substrate [47,48,49]. The general idea of this type of force detection with QTF is the enormous sensitivity of the oscillations to acting force. For a previously calibrated force sensor the acting force can directly be calculated from change in the oscillations. [26] A QTF can be used in both modes- the amplitude modulation (AM) or frequency modulation (FM). In AM mode the QTF is running in constant excitation mode on the natural resonant frequency and the deviation of the amplitude is detected and applied to calculate the change in force operating on the QTF. In FM mode the deviation of natural

resonance frequency is detected by changing the acting load. The last method is more complicated and a further need for complex equipment is in order in comparison to the AM mode. This is due to the fact, that the system requires constant feedback to see the change in resonant frequency of the QTF and to hold the oscillating amplitude constant. Depending on how the sharp tip is attached to the QTF, it is able to oscillate in both normal and shear mode. In the normal mode the resonator oscillates perpendicularly to the surface and in shear mode, the QTF oscillates parallel, as can be seen in Figure 2.

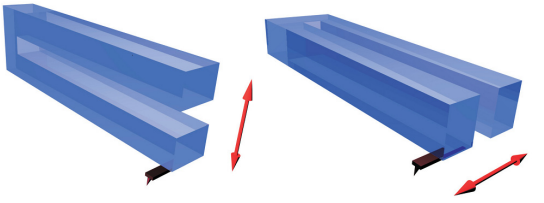

Figure 2. Normal (left) and shear (right) modes of the QTF force sensor.

To conclude, the combination of a high Q-factor resonator (>1000 for QTF) attached to a precise nanomanipulation platform positioned inside a SEM enables one to manipulate nanostructures and measure forces in the nN range in real time, which has a huge advantage over the AFM based manipulation method.

But still, in some cases the AFM based mechanical characterization can be quite useful. In the 3PB configuration, a smooth force-displacement curve can be obtained with AFM, which would be impossible with the QTF based manipulation method, because in the latter case, the tip is in constant motion and no stable contact between tip and NW can be established. This is a problem for pentagonal NWs, where the sharp apex is pointing upwards so slippage of the tip is simpler. There is a higher risk of the QTF sensor touching the surface of the substrate as well, as the etched holes may have depth in the range of the oscillating amplitude of the QTF.

3.1.2. Experiments

3.1.2.1. Manipulation of ZnO NWs for calculating static friction force distribution

The manipulation experiments were conducted on ZnO NWs, which were fabricated by the vapour transport method (VTM) [50] and the obtained structures had a well-defined geometry, with characteristically flat facets [51] and good mechanical strength for performing successful experiments. The ZnO NWs had length from 10 to 20 μm and diameter from 60 to 200 nm. The manipulations were performed inside the Tescan VEGA II SEM with contact AFM cantilever attached to the SmarAct SLC-1720-S nanomanipulator. The mechanical transfer method was applied for moving the NWs from the VTM substrate to the flat

silicon surface. A more detailed description of the experimental setup can be found in [52]. For manipulating a single ZnO NW on the silicon substrate, the following procedure was applied. The sample was visualized in SEM and proper ZnO NWs with suitable aspect rations, from 30 to 60, were chosen for manipulation experiments. NWs with such aspect ratios can easily be bent into complex shapes, as for smaller aspect ratio NWs the elastic forces are able to overcome the static friction and only trivial shapes (arc-shape) can be gained. After finding the suitable NW fitting the desired parameters, they were manipulated with the AFM tip into complex shapes. After removing the tip from the NW, the NW stays in the shape, it was manipulated in. This is due to the equilibrium between the elastic and static friction force. A number of different NWs were manipulated into different complex shapes and the static friction between the NWs and the silicon surface was calculated.

Firstly, there are a number of parameters necessary for applying the elastic beam theory for calculating the static friction distribution between the NW and substrate. One needs knowledge of the geometrical parameters, like diameter and length. Additionally, the elastic modulus must also be known. These parameters directly affect the interfacial forces acting at the surface of the NW and thus influence the mechanical performance of the NWs. The cross-section of the ZnO NWs in the manipulation experiment performed is hexagonal [53]. Elastic modulus of 58 GPa was chosen for the static friction calculation, as was measured in an earlier work [44]. Secondly, the proper skeletonization procedure must be

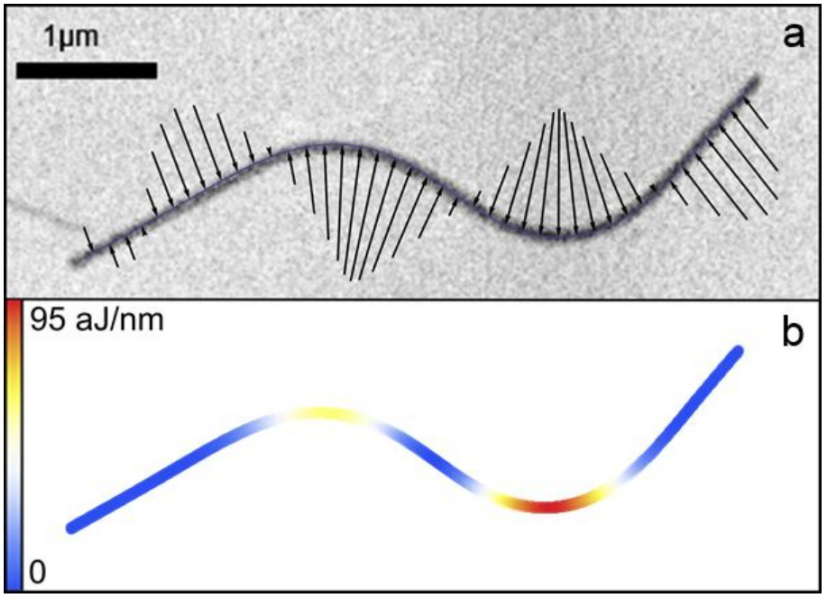

Figure 3. Static friction (a). Elastic energy (b). The total elastic energy in the bent NW is 0.14pJ.

carried out for extraction of the centerline of the NW for obtaining the local curvature distribution function. And finally, the static friction force distribution and the elastic energy distribution were calculated, as can be seen in Figure 3., if the local curvature distribution function is known. All the details related to the application of the elastic beam theory and additional details can be found in [54].

3.1.2.2. Manipulation of SiO_2 nanotubes

SiO_2 nanotubes were fabricated from Ag/SiO_2 core-shell NWs. Those core-shell NWs were produced by covering silver NWs with a SiO_2 layer by applying the sol-gel method. [55,56,57]. The resulting SiO_2 NTs are expected to have an amorphous structure. [58]. To obtain the empty shells, nitric acid was applied for etching the silver core. Then, the NTs were deposited via liquid droplet onto an AFM calibration grating where they dried for approx. a few minutes and were washed afterwards with deionized water.

The friction force between the NT (nanotube) and silicon surface was sufficient to hold the adhered section of the NT fixed during the bending experiments. The cantilever beam bending technique [59,60] described in experimental section was applied to half-suspended NTs. The shear mode of the QTF force sensor was applied in all the bending experiments. After concluding all the experiments the final sample was viewed under the HRSEM (high resolution scanning electron microscope) for measuring the outer and inner radii of each individual SiO_2 NTs studied in the cantilevered beam bending experiment. A typical SEM micrograph of a bent NT can be seen in Figure 4.

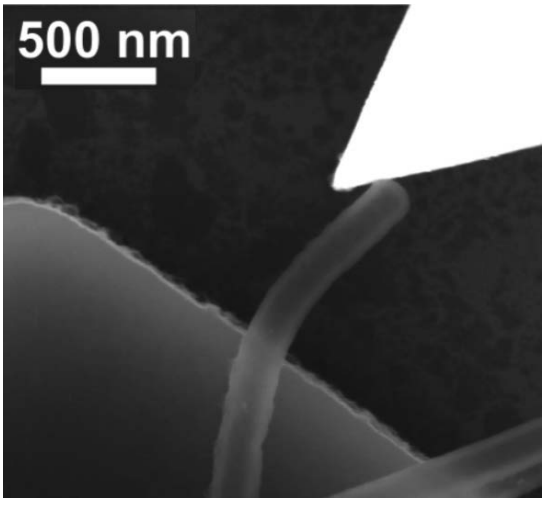

Figure 4. A scanning electron micrograph of a SiO_2 nanotube being bent by an AFM tip.

In total the cantilever beam bending technique was applied on 12 SiO_2 NTs and the measured value of the elastic modulus was fitted to the experimental force–distance curves obtained by the QTF by using the elastic beam theory. The measured average value of the elastic modulus was 24.5 ± 11.1 GPa.

3.1.2.3. Manipulation of Ag-SiO_2 core-shell nanowires

For studying the mechanical properties of individual Ag-SiO_2 core-shell NWs, the *in situ* SEM cantilevered beam bending test was applied. The NWs were deposited onto a transmission electron microscope (TEM) grid (Agar, UK) from methanol solution. The mechanical response was studied for two kinds of core-shell NWs, one having a "thick" and other having a "thin" shell. The "thick" and the "thin" structures had a shell thickness of 34±6 nm and 10±5 nm, respectively. For the "thick-shelled" core-shells an interesting effect of electron beam induced shape restoration was observed. If the structure was bent and the external force was removed rapidly, the structure restored its initial profile within minutes. If the beam was turned off, the restoration stopped and NW was "frozen" and as soon the beam was turned on again, the restoration continued from the last position. The latter was not seen for "thin-shelled" NWs. The restoration effect can be viewed a restoration of a viscoelastic material. [61] Experiments were conducted on nine Ag-SiO_2 core shell NWs and it was found, that full restoration takes place only, if the maximal bending curvature does not exceed 0.4 μm^{-1}.

An additional effect related to the mechanical properties of the core-shell structures was the high fracture resistance. For many of the NWs the maximal curvature reachable, before fracture, was approx. 2.1 μm^{-1}, resulting in a loop configuration, as can be seen in Figure 5.

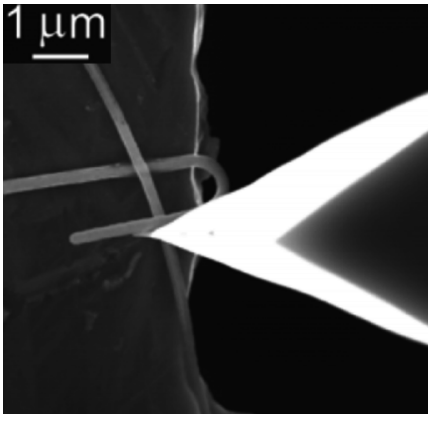

Figure 5. SEM micrograph of a Ag-SiO_2 core-shell NW bent to a high degree and showing high fracture resistance.

Such high fracture resistance was not observed for pure Ag NWs. [60], where typically the NWs were deformed plastically or were broken. The maximal mechanical stress in the Ag core of the core-shell NWs were estimated using the maximal bending curvature without fracture and it was shown, that the bending stresses can reach values of up to 15 GPa, which is almost twice as high as was measured for Ag NWs (8.5GPa).

The experimental conditions were simulated using the FEM and the mechanisms behind the shape restoration and fracture resistance were proposed. The details and results of the FEM simulations are presented in section 3.3.2.

3.1.2.4. Nanodumbbell formation on a flat surface by melting

The formation and tribological properties of Ag NDs produced by laser processing of corresponding metal NWs on oxidized silicon surface were studied.

Nanodumbbells were formed on a Si substrate by laser irradiation. As the NWs were irradiated, the energy of the laser light is absorbed and ends of NWs start melting and form a liquid droplet, which starts to grow in volume and will simultaneously move towards the center of the NW. As a result, the surface tension of the liquid Ag tries to minimize the surface area and forms a spherical droplet. The temperature in the middle part of the Ag NW is lower than the melting temperature and the internal crystalline structure is kept in tack. If now the structure would cool, the central part acts as a crystallization center and as a result, the molten ends will crystalize epitaxially, as defined by the central part. After the NW has solidified, there is elastic stress acting inside the NW due to the upward bending induced by the bulbs, trying to straighten the central part still attached to the surface. Also the axial stress induced by thermal contraction is acting in the system. If now the adhesion force in the central part between the NW and substrate is smaller than the elastic restoration force, the NW will be

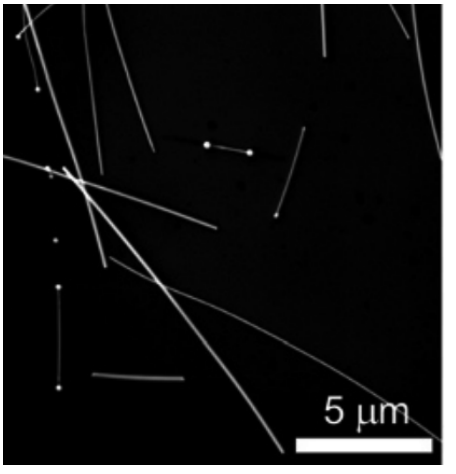

Figure 6. SEM micrograph of nanodumb-bells.

detached from the surface and will rest on the bulbs. The latter is confirmed in many cases by SEM observations, as can be seen in Figure 6. Exact mechanism of NWs complete detachment is rather complex and requires advanced computer simulations [62, 63]

For estimating the stresses induced by the solidified end bulbs, FEM simulations were conducted for two different types of configurations.

3.2. AFM based mechanical characterization of 1D nanostructures

3.2.1. Experimental setup

The mechanical characterization was performed with an atomic force microscope (AFM, Bruker Dimension Edge) under ambient conditions. In the AFM measurements, the built in optical microscope was employed for finding the correct positions of the Au NWs and plates previously visualized with HR-SEM. The NWs and NPs were visualized in the tapping regime (typically 10*10 μm^2 or 30*30 μm^2) of the AFM and after finding the proper nanoparticle a zoomed image (~3*3 μm^2) was obtained. The high-zoom image enables to position the AFM tip with a higher accuracy necessary for obtaining the correct force-displacement curves. The built-in software was then used for obtaining the force-displacement curves by pushing both the NWs and NPs downward at the overhanging site. After the mechanical testing experiments the AFM cantilever was characterized in the HR-SEM for obtaining all the geometrical parameters (tip radius, length, width, thickness) necessary for calculating the normal stiffness. For obtaining the sensitivity of the AFM cantilever a force-displacement curve was measured on the hard silicon substrate. This knowledge enables the decoupling of the raw AFM data into the corresponding displacement of the AFM tip and the Au NW. HR-SEM imaging was applied for determining the diameters of the NWs used in the 3PB and cantilevered bending experiments.

3.2.2. Experiments

3.2.2.1. Mechanical characterization of SiO_2 nanotubes

Both the 3PB and nanoindentation methods were applied with an AFM (Dimension Edge, Bruker) under normal conditions for measuring the mechanical properties of SiO_2 NTs.

The built-in optical microscope was applied for finding properly positioned SiO_2 NTs for conducting the 3PB and the nanoindentation experiments. Before the 3PB experiment an low-magnification AFM tapping-mode image of a NT suspended over a trench was obtained. (approx. 10×10 μm^2, Figure 8a). For having satisfactory accuracy at tip positioning for the force spectroscopy measurement a higher magnification (approx. 3×3 and 1×1 μm^2) image of the

NT were taken. A number of force–displacement measurements were obtained at the middle point of a suspended NT. Typically the measured curves were linear, and the loading and unloading curves coincide, as one would expect of purely elastic materials. A force–displacement curve was taken on the silicon surface for comparison (Figure 8b).

3PB test makes use of the elastic beam theory, which is sufficient for the analysis of the results in the elastic regime. The force–distance relationship linking the elastic and the tensile deformations of an isotropic elastic beam can be given as

$$F = \frac{192EI}{L^3}\delta(1 + \frac{A}{24I}\delta^2) \tag{1}$$

where A represents the area of the cross section and δ is the deflection of the center point of the beam. In the cylindrical shell case with outer and inner radii of, RS and RC, respectively one is able to get the following expressions of $A = \pi(R_S^2 - R_C^2)$ and $I = (\pi/4)(R_S^4 - R_C^4)$. In the linear case for relatively small deflections the equation for the elastic modulus reduces to:

$$E = \frac{FL^3}{192\delta I} \tag{2}$$

The raw AFM force-deflection curves are being used as the basis for gaining the corresponding deflection of the beam and the real force applied to it. From this, one is able to calculate the elastic modulus of the beam using Eq. 2.

Elastic moduli were calculated by Eq. 1 and Eq. 2. The results of the fitting are depicted in Figure 7. The initial section, i.e., the section of deflection having values lower than the characteristic inner radius of the NT, was used for fitting since the high load region would be incorrect due to the non-linearity and plastic deformation effect. Measurements were conducted on five NTs and the final results shown in Table 1.

Table 1. Comparison of measured NTs with different techniques.

Nr.	Outer diameter, nm	Inner diameter, nm	Elastic modulus from three point bending, GPa	Elastic modulus from nanoind., shell GPa	Elastic modulus from nanoint, Hertz, GPa	Elastic modulus, nanoind (FEM)
1	91	56	42.3	6.1	5.4	22.0
2	86	50	37.0	11.6	5.9	29.0
3	87	45	41.8	10.0	5.9	21.5
4	115	62	36.5	6.3	2.6	16.8
5	91	41	48.5	5.6	3.0	11.3

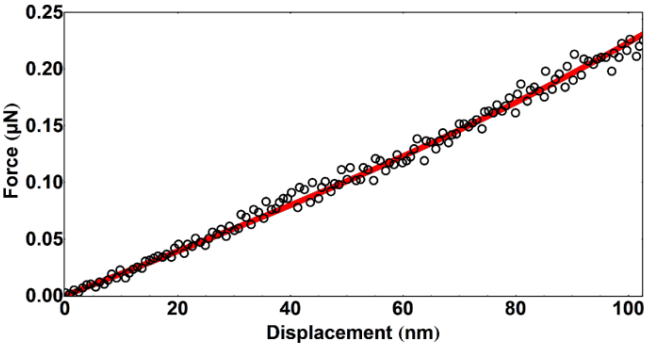

Figure 7. Fitting of three-point bending test of silica NT in AFM.

The nanoindentation measurements were conducted on the same NTs that were measured with the 3PB test. A chosen area of a NT lying on the substrate was visualized prior and after the nanoindentation measurement. Several force–displacement curves (approx. three) were obtained on a NT with an interval distance of approx. 1 μm. Typical force–displacement curve is visualized in Figure 8c. Only the initial linear section was used for the mechanical analysis.

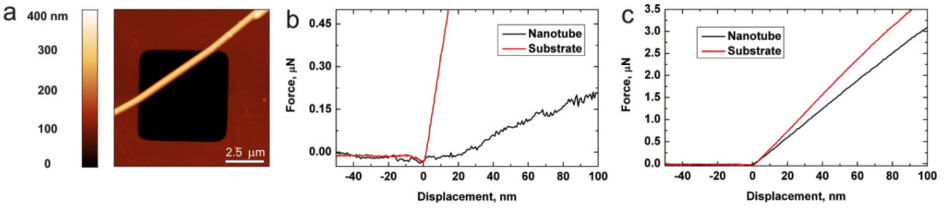

Figure 8. Three-point bending test and nanoindentation. AFM image of suspended silica NT (a); force–distance curve taken on the suspended part of the NT (b); nanoindentation force–distance curve taken on adhered part of the same NT (c).

The analysis of the nanoindentation test is more complex and it lacks direct analytical solutions. The existing models available in literature for indentation of a NT is limited to the thin-shell and membrane case. For the case of the thicker shells/NTs characterized in this work, the finite element method models were applied instead.[64] The experimental nanoindentation data from measurements was analyzed by using the FEM simulations and are discussed in section 3.3.4. where also the thin shell and Hertz models are taken into account.

3.2.2.2. Mechanical characterization of ZnO nanowires

Young's modulus is one of the most critical parameters for calculating the frictional properties of ZnO- SiO_2 interface. There are a number of works available, where the mechanical properties of such NWs have been studied. [35,65,66,67,68,69,70,71,72,73,74]. Sadly, most of the elastic modulus values

available in literature show a huge diversity, having values from few tens [e.g. 32,33,38,39] to hundreds of GPa [e.g. 34,40]. Even a clear dependence of mechanical properties on the diameter of the NW was shown [e.g. 34,36,75], and some do not [e.g. 35]. For this reason, it is clear, that each and every set of NWs used in experiments must be characterized prior.

The elastic modulus of ZnO NWs was characterized by the 3PB test. [76]. The results of the experiments of 21 ZnO NWs of varying diameters are shown in Figure 9.[77]

The size effect became important for ZnO NWs with diameters below 40 nm. The obtained values of Young's modulus are higher than others reported in literature. But the obtained results are have a better consistency with the bulk value of 140 GPa for ZnO and are in a good agreement with values reported by Chen et al [46] and Stan et al [49]. However, contrary to [46], the size effect observed in our case appears at smaller diameters. The measured elastic modulus with all the geometrical data obtained from SEM measurements was used as an input parameter for the FEM simulations related to the tribological properties are discussed in section 3.3.3.

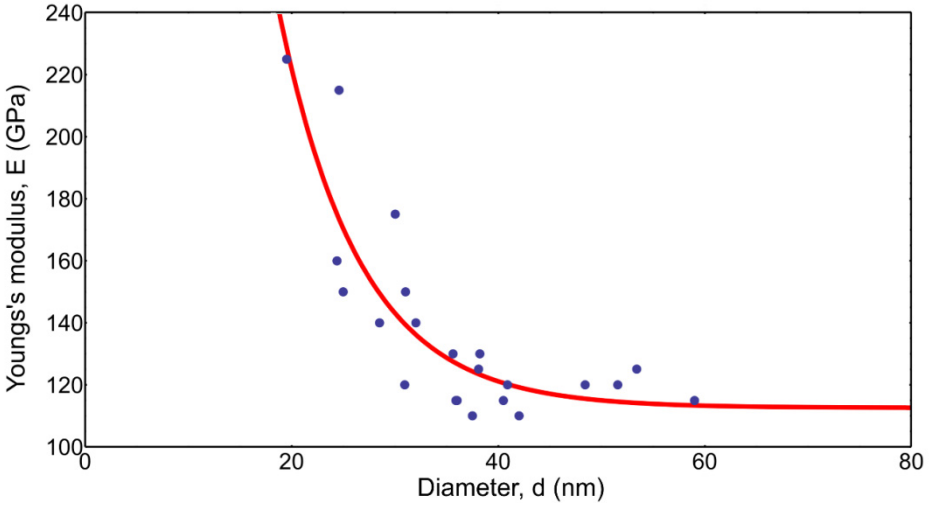

Figure 9. Elastic modulus vs. diameter of ZnO NWs measured with the 3PB technique.

3.2.2.3. Mechanical characterization of Au nanowires

The synthesized Au NWs and NPs (nanoplate) were drop-casted from ethanol solution onto the patterned silicon substrate by the laser lithography method. After the drop-casting procedure some of the Au NWs were either partly suspended over the rectangular holes or with the sides of the NWs fixed on the substrate by high adhesion forces (Figure 10a) or were positioned diagonally inside the i-pyramid with the ends of the NW being free (Figure 10b). The NPs were also randomly distributed on the substrate and only a fraction of them

were positioned half-suspended over the holes (Figure 10c). The 3PB method was applied for both the fixed and free end configuration of the Au NWs and the cantilevered beam bending technique was applied for the half-suspended NWs (Figure 10d). The analysis of the NPs was more complicated and direct classical methods were not applicable and so only the FEM numerical simulations were employed for their characterization.

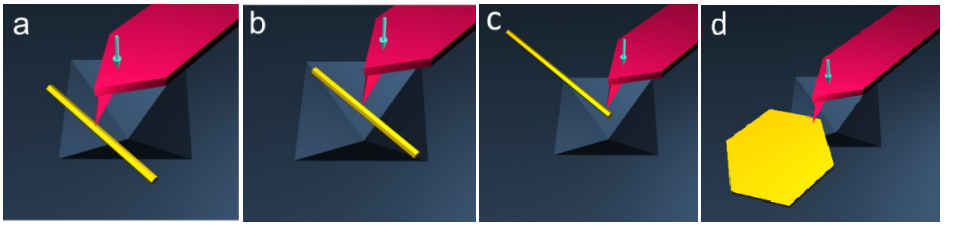

Figure 10. Scematics of different boundary conditions of Au nanostructures.

Prior to the mechanical characterization, the samples were visualized in a high resolution scanning electron microscope (HR-SEM) for finding the proper NWs and NPs in appropriate configurations.

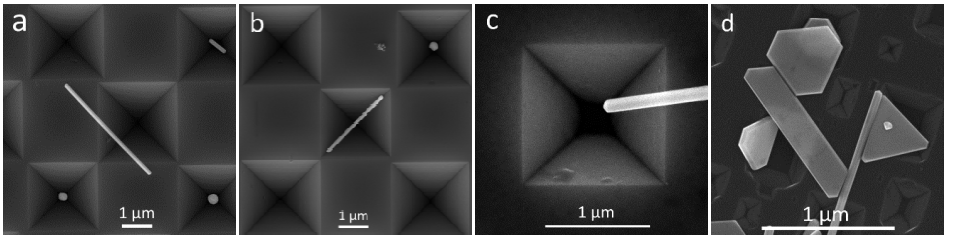

Figure 11. Gold nanostructures in different configurations.

The elastic beam theory is typically used for the analysis of elastic isotropic beams deformed by an external force. For the 3PB test configuration with free ends, the force-displacement relationship is governed by the following expression [78]:

$$F = \frac{48EI}{L^3}\delta \tag{3}$$

where δ is the displacement of the center point, L the length, E the Young's modulus and I the area moment of inertia of the beam.

The force-displacement relationship for the 3PB test with fixed ends, where both the elastic bending and tensile strain is taken into account, is given by Eq. 1.

For the cantilevered beam bending configuration, the force-displacement is given by the following relationship [69]:

$$F = \frac{3EI}{L^3}\delta \tag{4}$$

For a pentagonal beam, the area moment of inertia can be expressed as:

$$I = \frac{1}{96}\frac{(3-\sqrt{5})}{(3+\sqrt{5})}\sqrt{265+118\sqrt{5}}D^4 \tag{5}$$

where D is the apparent diameter of the beam measured from SEM micrographs.

In the linear elastic regime and small displacements, for both the free and fixed ends and the cantilevered configuration, the Young's modulus can be expressed as: $E = k_{TPB}\frac{L^3}{48I}$ and $E = k_{TPB}\frac{L^3}{192I}$, $E = k_{TPB}\frac{L^3}{3I}$ respectively, where k_{TPB} is the stiffness of the beam measured from the AFM bending experiments.

Due to the complex configuration of the experimental setup for the Au NPs analytical models cannot be directly applied resulting in the necessity of using numerical FEM simulations for calculating the Young's modulus of the plates.

Gold NWs and plates were randomly dispersed on the substrate surface. Only a fraction of the NWs and plates were positioned in the correct positions on the substrate with the i-pyramids. Each measured NW and NP was visualized both before and after the mechanical characterization with the AFM to check for any plastic deformation or defects induced by the AFM tip during the bending experiment. As a result, no differences between the images before and after experiments were found. Thus confirming that the deformation of the NWs and plates was purely elastic and no plastic deformation occurred during the bending tests.

Several force-displacement curves were obtained and the response was typically linear. The linear part of the indentation curve was used for calculating the Young's modulus using the theoretical curves governed by Eq. 1., 3. and 4. The Young's modulus was measured for 21 Au NWs with fixed ends configuration, for 14 NWs in the free ends configuration and for 3 NWs in the cantilevered configuration. The measured NW had diameters in the range from 100 nm to 150 nm with a median value of 124 nm. The median elastic modulus for the fixed and free ends configuration was 88+–20 GPa and 87+–16 GPa, respectively. For the cantilevered configuration the elastic modulus had a median value of 63+–16 GPa. The Young's modulus values obtained from the bending experiments on Au NWs can be seen in Figure 12., where no diameter dependence can be recognized, as the diameters of the NWs are mostly above 100 nm and no size-effect is to be expected in that range. The slightly higher (approx. 10%) Young's modulus obtained from the 3PB experiments could be explained by the anisotropic structure of the pentagonal NW. It was shown by Mets et al. [79] that the peculiar structure of pentagonal NWs could lead to a higher overall stiffness of the NW as the internal structure of the NWs is not taken into account. The lower elastic modulus values for the cantilevered bending configuration could be explained by the slippage of the AFM tip during

the bending experiments. This slippage cannot be directly taken into account, as it may vary for different experiments.

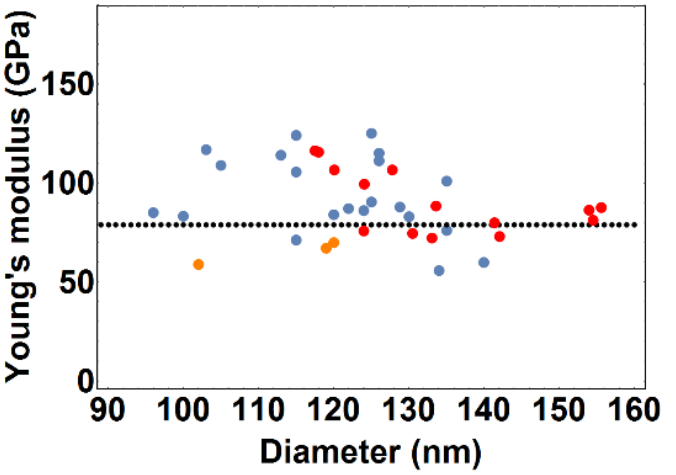

Figure 12. Young's modulus for three configurations: blue- fixed, red- free, orange- cantilevered configuration.

The plastic yield of the Au NWs was measured for 15 NWs in the fixed ends 3-point bending configuration and for 3 NWs in the cantilevered bending configuration (Figure 13.) with typical diameter ranging from 100 to 130 nm. Most technical details are the same as for the Young's modulus measurement. The deflection was increased for overcoming the plastic limit and inducing plastic deformation in the Au NW. The 3-point bending and the cantilevered bending measurements resulted in a median plastic yield value of 1.45 GPa and 0.94 GPa, respectively. The high yield strength value from the 3-point bending experiments indicates, that the NWs were of high quality and with a relatively low concentration of defects as was indicated in the works conducted by Wang et al. [80] The lower yield strength values from the cantilevered beam bending experiments may also indicate slippage of the AFM tip.

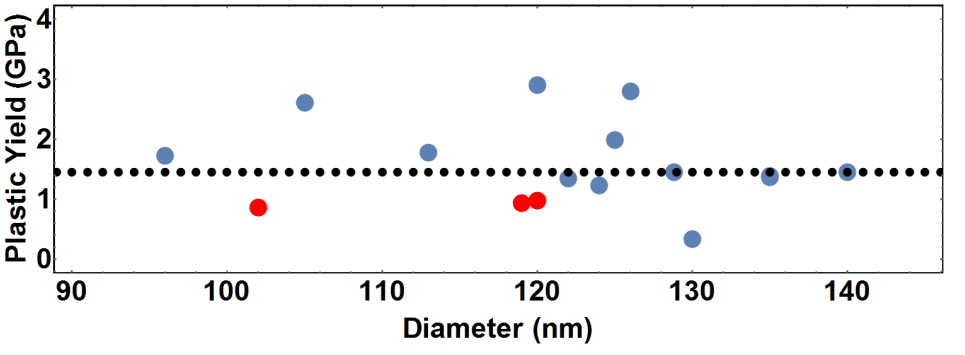

Figure 13. Plastic yield distribution of Au NWs.

Plastic yield measurements for the free ends configuration were not conducted. As the NW is pushed downward it slides freely on the sides of the i-pyramids and before the plastic limit is reached, the NW is already pushed against the bottom of the i-pyramid and as a result no measurements can be performed.

3.3. Finite element method simulations of studied 1D nanostructures

3.3.1. Formation of Nanodumbbells

To reveal the stresses induced in the nanodumb-bell ND formation process first we need to roughly estimate all the factors involved in the detachment process of the ND. These forces are induced by the adhesion force between NW and substrate, the elastic force of the deformed NW due to bulb formation and the thermally induced stress by cooling.

The contact pressure caused by adhesion forces between one of the facets of the NW and the substrate can be estimated as [81]:

$$P = \frac{A}{6\pi D^3} \tag{6}$$

where D is the cutoff distance and A is the Hamaker constant between the Ag/SiO_2 contact system. The Hamaker constant of the contacting interface of Ag/SiO_2 can be calculated by: $A = \sqrt{A_{Ag} A_{SiO_2}}$, where A_{Ag} and A_{SiO_2} are the Hamaker constants of Ag and SiO_2 respectively. The constants have values of $3.72*10^{-19}$ J and $0.62*10^{-19}$ J, for Ag and SiO_2, respectively and the cutoff distance is D=0.2nm [44]. From the equation one can calculate, that the contact pressure between the Ag/ SiO_2 system is approx. 1GPa, which is the minimal pressure need to create new surfaces.

In addition, the thermal stress induced by cooling can also play an important role in the separation process. The thermal strain can be calculated by the following expression:

$$\varepsilon_{th} = \alpha_{Ag} \Delta T \ ,$$

where α_{Ag} is the thermal expansion coefficient and ΔT the difference between the final and initial temperatures of the Ag ND. For silver, the coefficient has the value of $19.7*10^{-6}$/K [82] and taking the temperature difference of 680K, the stress induced by the calculated strain of 1.34% is approx. 1.1 GPa. And as a result, all the elastic stress components act in the surface separation process, which in general can be envisioned as a surface crack propagation phenomenon.

A FEM simulation was prepared to study the elastic response of the Ag ND nanostructure interaction with a flat SiO_2 substrate. For revealing the stresses acting at the interface, a finite element method (FEM) simulation was applied

for the analysis of the mechanical behavior of an Ag ND interacting with a flat surface. The simulation model contained a dumbbell geometrical object lying on a flat rectangular block. The length between the two bulbs making the ND was held at a constant value of 2 microns and the simulation was conducted with a radius of the two bulbs of 175 nm. Two systems were considered, the early stage of dumb-bell (DB) formation, where the adhered side length was 1 μm and a later stage, where most of the Ag NW between the bulbs is detached and length of the adhered part was 10 nm, as can be seen in Figure 14.

At the interfacial surface separation edge, the calculated elastic stresses were concentrated and could reach value of up to 0.5 to 4 GPa, which can already be sufficient for the separation of the two interfaces. One can see that as the length of the adhered part decreases, the elastic stress does so as well leading to the conclusion, that only short NDs have the possibility to detach from the substrate in total.

There are a number of interesting aspects, which should have been taken into account in the FEM models of the NDs. Firstly, the idealized case was studied here, where the bulbs were considered as spherical entities. The wetting of the molten Ag interacting with the SiO_2 substrate is not taken into account and as a result to some extent, the real contacting surface is not taken into account leading to some errors in the FEM simulations. But as the difference in height is less than 10 nm, it should not affect the end result to any extent. Secondly, the calculated stresses are always affected by the mesh size of the model. In this case, several simulations with varying mesh sizes were conducted and only a small deviation less than 10% was detected between the different mesh sizes. So generally, the obtained results can be trusted with quite high certainty. Thirdly, the idealized FEM model can only to a certain degree mimic the conducted experiments, as realistic defect distribution inside the studied material cannot be directly taken into account. Also the real contact area, not the apparent one,

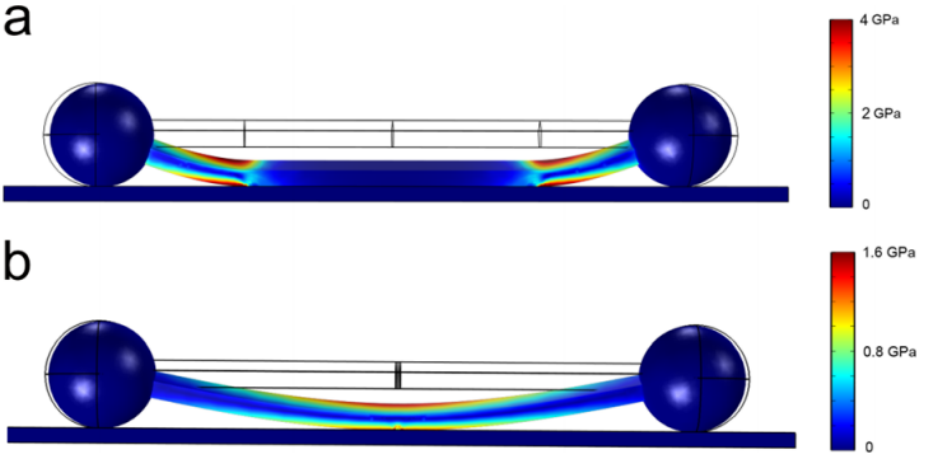

Figure 14. FEM simulations of elastic behavior of a ND adhered to a surface. a) adhered length 1 μm; b) adhered length of 2 μm.

cannot be taken into account. So still more advanced models should be applied. But to a certain degree, the FEM modeling is able to give more insight into the studied phenomenon and is able to describe the latter in a more detailed way, as the theoretical calculations from before are in quite a good agreement with the stresses calculated in the FEM simulations. [64]

3.3.2. Ag-SiO_2 core-shell nanowires: viscosity-elasticity

The FEM method was applied to estimate the viability of the explanation of the core-shell NW restoration effect, and to calculate the viscosity of the shell under e-beam radiation. Geometry of the studied core-shell NWs was replicated fully. The length core-shell radii were obtained from SEM micrographs. More details about the simulation can be found in [57]. Viscosity η of the core-shell was varied in FEM calculation for finding good fit between experimental and simulated relaxation curves.

Calculated η values (from 2×10^{11} to 2×10^{12} Pa·s/7 $\times 10^{11}$ Pa·s in average) were seen to be very near to glass transition viscosity of solids, from where one is able to conclude that e-beam is able to induce glass transition in SiO_2 subjected to an external load.

Simulations were conducted also to illustrate the mechanical stress distribution at the vicinity of the fixed part of the NW. The simulations were performed with Ag NWs and Ag-SiO_2 core-shell NWs and it was shown, that the von Mises stresses at the fixed boundary can exceed the strength of Ag. The stress distribution for Ag can be seen in Figure 15.

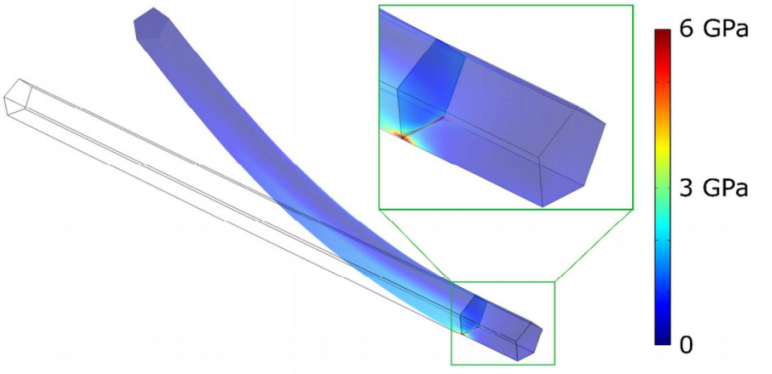

Figure 15. Von Mises stress distribution of a purely bent Ag NW fixed partly on a substrate.

But when the SiO_2 layer is present, the stresses are concentrated at the shell and relieved in the core, as can be seen in Figure 16. Thus, the shell is able to protect the silver core in bending tests.

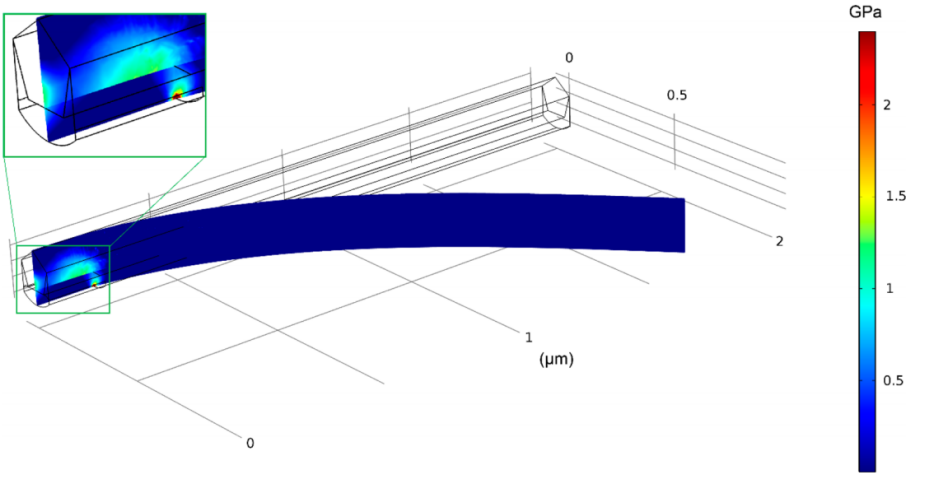

Figure 16. Von Mises stress distribution of a purely bent Ag-SiO_2 core-shell NW fixed partly on a substrate.

3.3.3. ZnO NWs: static friction

The struggle between the elastic NW strength during cantilevered bending and NW/substrate contact strength can lead to either the fracturing or the displacing of the studied NW. The "pick-and-place" method was used by destroying the suspended part of ZnO NW and moving it to a suitable place in high vacuum to enable as fresh contacts as possible. This enabled the precise control over the length of the adhered part of the NW.

After the broken NW was positioned on a location on the surface, static friction force measurements were conducted. Every experiment began with the positioning of the broken ZnO NW a preferred location, ensuring that in each experiment, the contacts are fresh.

The measurement of static friction force in the bending experiment typically relies on the elastic profile of the ZnO NW in the ultimate bending state just before the displacement of the fixed part. In the previous articles dealing with the calculation of the static friction force from the "most bent state", all the stresses at the interface and the related static friction force were thought of as linearly distributed in the fixed part [30, 31]. But for a more realistic approach, a novel FEM model was prepared and designed. For all the ZnO NWs that were manipulated and displaced in the measurements for examining the stress distributions in NW/substrate interface more correctly, a novel FEM model was applied. The ZnO NW was designed as a prismatic elastic cantilever with a realistic hexagonal cross-section. For simulating the NW/substrate contact in a static friction situation, the ZnO NW is loaded from one end and the adhered part is statically fixed. All the geometrical parameters of the NW, the length of the fixed part, the final deflection and the point of external bending load applied to the NW were gained directly from the experimentally measured NW in SEM.

The elastic modulus values were calculated separately for every simulation with a different NW and were based on the analytical equation obtained from the AFM measurements as can be seen in Figure 8.

The FEM model had of two primary parts: the hexagonal ZnO NW and a cylinder, which had the role if the AFM tip. The ZnO NW chosen to consist of In the two subdomains: the part being fixed on the surface and the suspended part above the trenches. In the framework of the Solid Mechanics node the the Linear Elastic Material module was chosen for all domains. The mesh for all the domains was custom designed. The adhered boundary of the ZnO NW had a mesh density of $2 \cdot 10^{17}$ elements/m^2. The density for the adhered part was chosen to consist of at least 4 elements in the lateral direction, as it corresponds to the actual surface roughness at the scale of the width of the NW side. The fixed part of the ZnO NW consisted of $4 \cdot 10^{25}$ elements/m^3 and was made out of prismatic elements. The suspended part was meshed by the default setup of Comsol. Approx. 10^3 elements made the whole mesh, depending on the size of the NW. For having consistency between different simulation parameters and results of each experimental setup, the mesh for the contact interface was changed manually. It was meshed as a $2 \cdot N$ matrix having quadrilateral elements, where N is the total number of mesh elements along the longer side of the ZnO NW. N was gained by multiplying the element density with the length of the ZnO NW, having a value of 1.5 elements/nm. For running the simulation a number of boundary conditions must be added. A facet at the part of the NW/substrate interface was fixed in the 3D. A contact boundary condition between the cylindrical probe and the bent part of NW was set and also the static motion of the cylinder, relative to the fixed part of the ZnO NW was set. The simulation was run and the bent configuration was gained, obtaining all the mechanical properties needed for analysis of static friction. From the calculations, the traction force at the interfacial boundary was obtained and shown on a 2D plot and on the basis of this distribution; the maximal interfacial strength can be calculated.

The FEM simulations showed an immense deviation from the linearly distributed stresses assumed in previous works. From the FEM model one could see, that the force distribution in the contact zone between the deflected ZnO NW and a flat surface is non-uniform and the highest interfacial shear stress is concentrated the vicinity of the boundary of the adhered and suspended domain of the ZnO NW (Figure 17.).

As a main result, one can see that the overcoming of static friction is more like a crack formation phenomenon at the point of maximal interfacial stress at the NW/substrate boundary. The start of a crack formation will rapidly propagate along the whole interface and as a result, the NW will be displaced. So in terms of this new model, static friction is basically the highest interfacial shear strength just before complete displacement. From this, one can see, that the static friction force will be much higher than the previous models estimated. This can also be seen when the maximal shear stress is calculated from the simplified model used in [31] gave 31MPa and for the case in Figure 17, the

FEM model predicts 1.8GPa. To summarize, the total median value for the interfacial shear strength calculated using FEM model for 16 ZnO NWs was 1.3 ± 0.7 GPa. This result can already be compared with the bending strength of ZnO NWs.

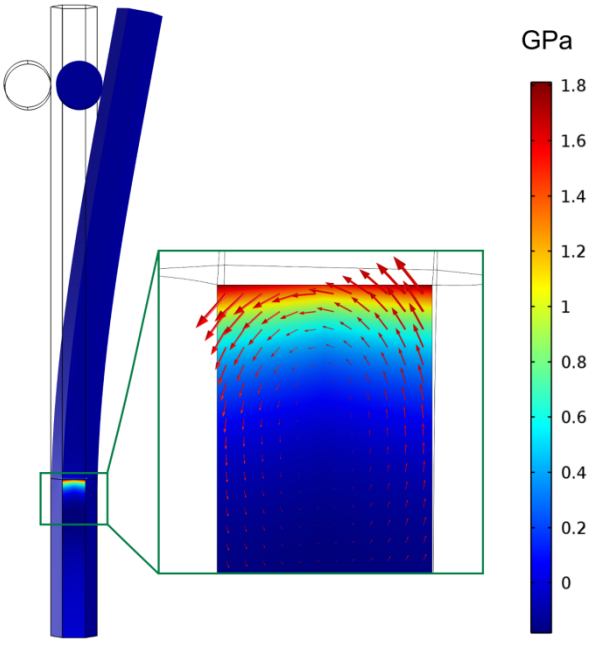

Figure 17. Interfacial shear stress distribution of a purely bent ZnO NW calculated from FEM simulations.

One might think that the high values obtained from FEM simulations and the new model is not correct, but the validity of the new model is supported by experimental results.

First, the degree of bending of the ZnO NWs in both the strength and static friction force measurements is comparable. This can mean that the detachment of the NW from the substrate and the mechanical breaking of NW are two completely different competitive actions and must have comparable values.

Second, the new model clearly shows, that static friction force no more depends on the length of the fixed part and it was indeed shown experimentally. It was possible to successfully manipulate a ZnO NW from its starting position without mechanically breaking it. This means that the strength of the contact was lower than the strength of the NW. As the shear strength during bending was overcome, some small part of the fixed part was released, but the whole NW was still held on the substrate. (Figure 18.)

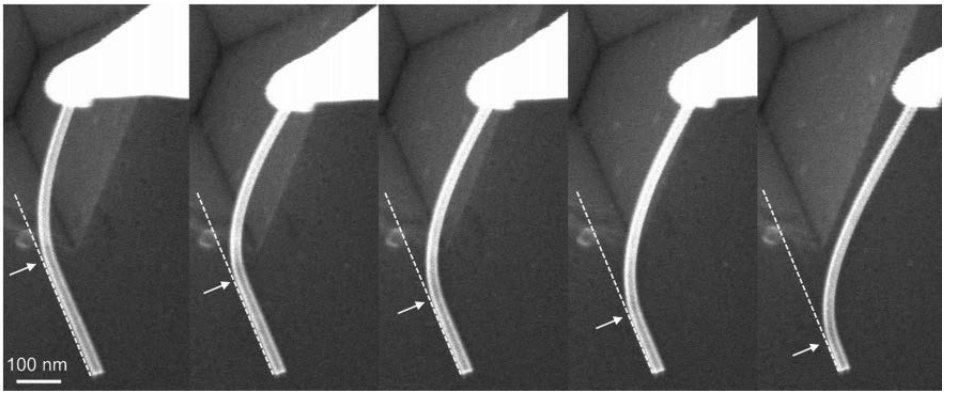

Figure 18. Gradual bending of a ZnO NW by AFM tip on a Si flat substrate.

As the tip moved at a constant rate transitions between the adhered situations were rapid making it possible to do five different measurements of shear strength for every case of the same NW. Each step happened at almost the same bending deformation of the NW and the calculations from the FEM model gave shear strengths values of 5.7 / 6.6 / 6.9 / 5.7 / 5.1 GPa, in the different points. The small differences in shear strengths indicate that the NW/surface strength is a characteristic value for the interface and is not dominated by random defects on the surface.

Therefore, the new FEM based model is able to more precisely determine the tribological properties of nanoscale interfaces and the simplified model previously used underestimates the stresses at the NW/substrate interface as the differences increase with length of the adhered part. [77]

3.3.4. SiO_2 nanotubes: mechanical properties from simulation

The experimental nanoindentation raw data was analyzed by applying the FEM simulations. At a constant indentation depth of 5 nm, the shell was deformed. This low indentation depth is due to the fact, that the initial section of the force-displacement curve corresponds to the elastic regime of the material and therefore the experimental results can be compared to the elastic results from FEM simulations. Geometrical parameters of the nanoindenter and each of the individual shells were measured from HRSEM micrographs. A snapshot of a FEM simulation result of the nanoindentation experiment is shown in Figure 19.

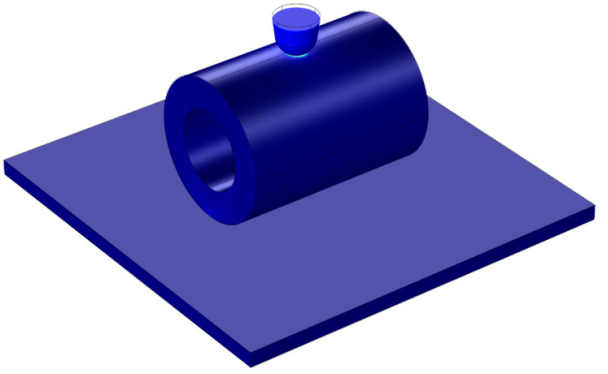

Figure 19. FEM simulation of a SiO_2 NT nanoindentation.

For gaining further insight also the thin-shell and Hertz models were applied for comparing the results. The thin-shell approach allows one to neglect the indentation of the surface and the tip geometry by taking into account only the membrane-like compression of the shell. The force–displacement relationship for the thin-shell approximation is commonly written as follows:

$$F \cong CE\frac{t^{5/2}}{R_S^{3/2}}\delta \tag{7}$$

where the thickness of the shell $t = R_S - R_C$ and C is a prefactor which value depends on the boundary condition but has a typical value of C = 1.2 [83].
On the other hand, the Hertz model [84] is able to describe the tip deformation and is not able to take into account the membrane like deformation of the shell. A sphere on a half-space is determined by the following force–distance equation:

$$F = \frac{4}{3}E^* R^{0.5}\delta^{1.5} \tag{8}$$

where E^* is the reduced Young's modulus and R is the effective tip radius.

According to FEM simulations, in case of nanoindentation of thick-walled SiO_2 NTs there are both compression and indentation present. Thus, both models underestimate the Young modulus as can be seen from Table 1.

3.3.5. AuNWs: mechanical properties from simulation in different configuratons

On the basis of the HR-SEM micrographs, the geometry of the experimentally characterized plates was measured in detail. The thickness was obtained from the AFM topography images of the plates. In the FEM simulations all the real experimental conditions were replicated: a gold plate was lying on a hard silicon surface and was indented by a fixed displacement applied onto a circular cross-section area on the NP, simulating the downward displacement with the AFM tip of the overhanging part. The coordinates of the position of the indenter were chosen to match the position of the AFM tip in the bending experiments. Corresponding force-displacement curves obtained from FEM simulations were compared to the AFM force-displacement measurements and by varying the Young's modulus in the simulations both the force curves were made to fit each other. As a result, the elastic modulus of the individual Au NPs was determined. Measurements were conducted on 3 Au NPs. The FEM simulations (Figure 20.) resulted in the elastic modulus with a median value of 79 GPa, which corresponds exactly to the bulk value for the Young's modulus of Au.

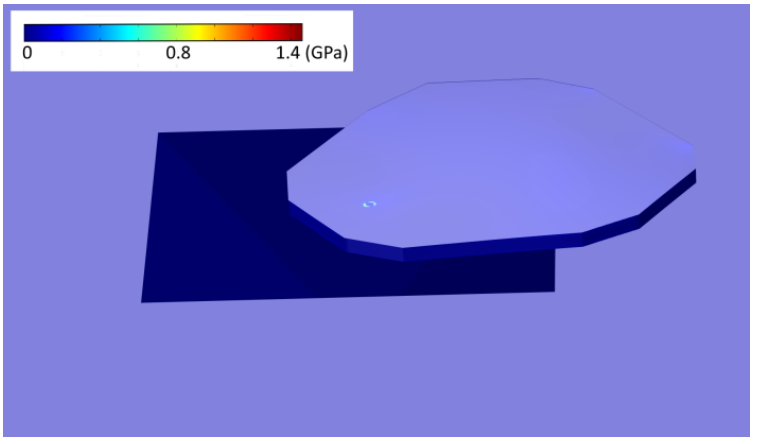

Figure 20. FEM simulation of bending of an Au nanoplate.

For gaining further insight into the effect the boundary conditions might have on the mechanical response of suspended nanoparticles, finite element method (FEM) simulations were generated to investigate the elastic behavior of Au NWs structures interacting with the substrate containing i-pyramids. The model was based on the real experimental configurations: the 3PB configuration with free and fixed ends and the cantilevered beam bending configuration. The model consisted of a pentagonal Au NW with a diameter of 103 nm, Young's modulus of 116 GPa and length of suspended part of 1.6 microns. For ensuring a comparable result all critical parameters were kept the same for both the 3 point bending simulations (deflection, mesh size, etc.). For the cantilevered beam bending configuration, the diameter and the elastic modulus and the displacement

of the free end was the same as for the 3PB configuration, but the length of the overhanging part was half of the length of the other configurations. This was done to keep the point of maximal deformation at the same distance from the ends of the NWs used in 3PB simulations and keep the simulation results comparable. The results of the simulations can be seen in Figure 21., where the distribution of internal stresses is visualized for each configuration.

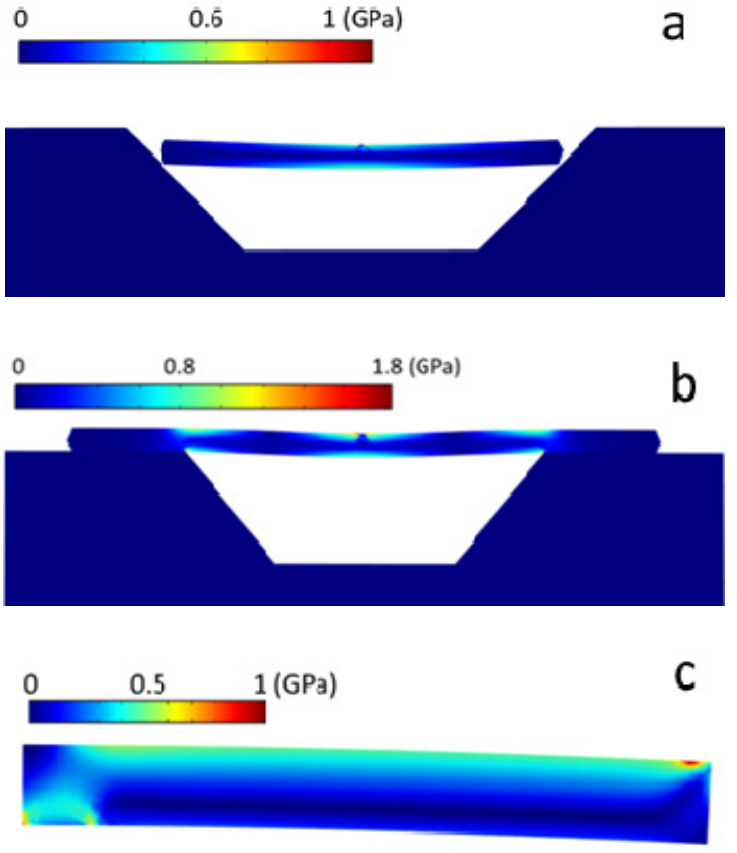

Figure 21. Von Mises stress distribution in three boundary conditions: a) free ends 3PB, b) fixed-ends 3PB and c) cantilevered beam bending.

The simulation revealed intrinsic stress distribution of the different configurations and a key noticeable difference is the large stress exhibited at the fixed boundaries of the cantilevered and fixed 3PB configurations. This high stress at the interface might also be high enough to induce plastic failure of the NW during bending. For the cantilevered bending experiment, that is quite obvious, but for the fixed 3PB configuration the stress at the middle point must be higher than at the fixed interface. This fact is also supported by the experimental findings, as the NW always broke from the center. As this cannot be seen in the simulations, because the stress at the center was lower than at the edges, which

indicates that in the experiments the “sharp” edges of the i-pyramids might not be that “sharp.” As the realistic shape of the edges cannot directly be taken into account, it is the cause for the high stress values in the simulations at the i-pyramid edges. The high stress at the edges of the NWs can be avoided in the free 3PB experimental configuration, as the ends are not fixed and exhibit lower tensile stress. This fact is also supported by the simulation results, as the maximal tensile stress along the NW for the fixed and free configuration was approx. 1.9 GPa and 1.2 GPa, respectively, which means, that the fixed configuration will reach the yield strength value at a lower deflection of the center point. The cantilevered beam configuration exhibited an intermediate tensile stress value of 1.5 GPa, at the same deflection. From the latter one can conclude that the free ends bending configuration might be most favorable for the mechanical characterization of NWs.

A critical factor in the nanoscale characterization of mechanical properties using the 3PB and cantilevered bending configuration is the static friction/ adhesion force acting at the interface between the NW and the substrate. If the adhesion force is too low, one is unable to perform such experiments, as the NW will overcome the adhesion force and displaces during experiment. As a result the measurements cannot be used for calculating any mechanical properties. In the case of Au NWs on the silicon substrate the adhesive properties were also investigated by means of theoretical calculations and FEM modeling. The method for calculating adhesion or van der Waals forces between the facet of the NW and the underlying substrate can be found in [81]. For the two surfaces in contact Eq. 6. is applied.

The Hamaker constant for the system can be calculated from the following expression:

$$A = \sqrt{A_{Au} A_{SiO_2}},$$

where A_{Au} is the Hamaker constant of gold and A_{SiO_2} is the same for SiO_2 with values $4.0*10^{-19}$ J and for SiO_2 is $0.62*10^{-19}$ J respectively and the cut-off distance is approx. 0.2 nm.

Using Eq 6. the calculated interfacial pressure for the system is approx. 1.04 GPa, which is the minimal value of pressure necessary to separate the two interfaces.

From the simulations with both the cantilevered beam and fixed 3PB configuration the simulated/calculated traction forces acting on the interface are an order of magnitude lower than the theoretically calculated adhesion force acting on the same surface area, which means that during bending experiments, the Au NWs cannot be detached without breaking them.

4. SUMMARY

A number of important issues concerning mechanical and tribological properties and behavior of 1D nanostructures were studied within the framework of the thesis. Main activity and the novelty aspects are summarized below.

First, tribological aspects of 1DNS manipulated on a flat substrate were considered. In particular:

- Nanowire elastically bent of a flat substrate is highly attractive for nano-tribological studies as profile of nanowire can be used for extracting frictional data without using external force sensors. In order to improve accuracy of the method, a novel analytical method was developed for the calculation of distributed static friction in elastically bent nanowire resting on a flat substrate. Unlike previously available methods, new model provides more realistic force spectrum and comply with boundary conditions. The method was successfully applied for calculation of distributed static friction in ZnO nanowires bent into arbitrary shapes in AFM manipulations on a Si substrate.
- A novel FEM model was developed for configuration in which part of the nanowire is resting on a flat substrate while other part is suspended over the trench. Measurements consist in bending the free end until fixed part is displaced. The bending profile prior the displacement of fixed part is used for calculation of force acting on a fixed part. In older models static friction was considered to be uniformly distributed in adhered part. The new model considered overcoming of static friction as a highly localized process similar to crack formation. It was shown, that existing models severely underestimated static friction, while novel model provides more realistic results.
- Dynamic FEM model of Ag nanowire that is being melted from both ends while resting on a flat substrate was created. It was shown that mechanical stresses, generated in nanowire due to the fact that molted ends form rounded bulbs, are able to overcome the adhesion between nanowire and silicon substrate. As a result, a configuration is achieved where only the end-bulbs of the obtained nanodumbell are in contact with the surface while intact midpart is suspended above the substrate. Such structure and configuration is highly attractive for tribological measurements as it can be easily manipulated due to the small contact area and at the same time it preserves all benefits of 1D geometry.

Further, mechanical properties of 1DNS were considered:

- Elastic properties of tubular 1DNS with thick walls were treated both experimentally and theoretically.
  - Elastic modulus of SiO_2 nanotubes was measured by three different methods including cantilever beam bending, nanoindentation and three-point bending tests. Three-point bending tests were found to be the most appropriate method for measuring the Young's modulus of thick-walled tubular 1DNS.

- FEM model was created to investigate the behavior of tubular 1DNS in nanoindentation test. It was shown there are both compression and indentation present. Thus, neither of existing models where walls of nanotube are considered either as a thin membrane or rigid wall cannot be used for given system as they underestimate the Young modulus.

- FEM model of composite core-shell nanowire consisting of elastic core and viscous shell was created to simulate the behavior of Ag/SiO_2 core-shell nanowire in bending test under electron beam irradiation. By fitting the experimental result with FEM model it was found that even at moderate current and voltage e-beam is capable of inducing glass transition in amorphous oxide shell.

Finally, two variations of three-point bending test of Au nanowires were compared: freely sliding ends and rigidly fixed ends. The effect of different boundary conditions on experimental results was determined and the adhesion forces acting between Au and substrate were estimated using the FEM modeling.

In total, it was demonstrated that FEM is a powerful method for studying mechanical and tribological properties of nanoscale systems when used in combination with experimental results.

5. SUMMARY IN ESTONIAN

Ühedimensionaalsete nanostruktuuride tribomehaanilised omadused: lõplike elementide meetodi simulatsioonidega toetatud eksperimentaalmõõtmised

Väitekirja raames uuriti mitmeid olulisi küsimusi, mis käsitlevad 1D nanostruktuuride mehaanilisi ja triboloogilisi omadusi ja käitumist. Põhitegevused ja uudsed aspektid on esitatud allpool.

1DNS elemente manipuleeriti tasasel pinnal ja analüüsiti vastavaid triboloogilisi protsesse. Alljärgnevalt tuvastati:

- Tasasel pinnal asetsev elastselt painutatud nanotraat on väga oluline nanotriboloogilistes mõõtmistes, kuna võimaldab nanotraadi profiilist lähtuvalt leida alusega seotud triboloogilised väärtused ilma välist jõusensorit kasutamata. Meetodi täpsuse parandamiseks töötati välja uudne analüütiline meetod, mis võtab arvesse staatilise hõõrde jaotuse tasasel pinnal asetseva elastselt painutatud nanotraadil. Erinevalt varasematest meetoditest pakub uus mudel realistlikuma jõuspektri ja arvesteb ääretingimusi. Meetodit rakendati edukalt staatilise hõõrdumise arvutamiseks ZnO nanotraatide korral, mis olid ränialusel AFM-i teravikuga manipuleerimisega suvalisse kujusse painutatud.
- Uus FEM mudel töötati välja sellise konfiguratsiooni jaoks, kus osa nanotraadist toetub lamedale substraadile, samal ajal kui teine osa on vabalt üle serva. Üleulatuva vaba otsa painutatakse alusele fikseeritud osa nihkumiseni. Registreerides paindprofiili vahetult enne fikseeritud osa nihkumist, saame sisendi fikseeritud osa mõjutatava jõu arvutamiseks. Vanemate mudelite puhul võeti eelduseks staatilise hõõrdejõu ühtlast jaotust fikseeritud osale. Uue mudeli puhul näidati staatilise hõõrdumise ületamist väga lokaliseeritud protsessina, mis sarnaneb pragude tekkimisega. Näidati, et olemasolevad mudelid on staatilisest hõõrdumise rolli tunduvalt alahinnatud, samas kui uus mudel pakub reaalsusega paremat kooskõla.
- Töötati välja dünaamiline FEM-mudel lamedal aluspinnal asetsevast mõlemast otsast sulanud Ag nanotraadi kirjeldamiseks. Näidati, et nanotraadis tekitatud mehaanilised pinged on tingitud asjaolust, et sulanud otsad moodustavad ümarad elemendid, mille tulemusena on võimalik ületada nanotraadi ja ränialuse vahelist adhesiooni. Selle tulemusena saavutatakse konfiguratsioon, kus ainult saadud nanoosakeste otsaelmemendid puutuvad kokku pinnaga, samas kui keskosa on pinna kohal. Selline “hantlisarnane” struktuur ja konfiguratsioon on tribologiliste mõõtmiste jaoks äärmiselt atraktiivne, kuna seda saab hõlpsasti manipuleerida väikese kontaktiala tõttu ja samal ajal säilivad kõik 1D geomeetria eelised.

Lisaks uuriti alljärgnevid 1DNS mehaanilisi omadusi:

- Karakteriseeriti paksude seintega torukujuliste 1DNS elastseid omadusi kasutades nii eksperimentaalseid kui ka teoreetili meetodeid.
  - SiO_2 nanotorude elastset moodulit mõõdeti kolme erineva meetodi abil, kasutades konsooltala painutamist, nanoindetatsiooni ja kolme punkti paindekatseid. Tuvastati, et kolme punkti paindekatse on kõige täpsem meetod paksuseinaliste torukujuliste 1DNS elastusmooduli mõõtmiseks.
  - Loodi FEM mudel torukujulise 1DNS käitumise uurimiseks nanoindantsatsiooni testis. Näidati, et protsessi käigus toimub materjali kokkupressimine ja kuju muutus. Seega ei saa ühegi olemasoleva mudeli puhul, kus nanotorude seinteks on kas õhuke membraan või jäik sein, sellist süsteemiga materjali karakterisseimisek kasutada, kuna nad alahindavad elastsusmoodulit.
- Loodi FEM mudel, mis kirjeldab elastsest südamikst ja viskoossest kestast kooseneva Ag / SiO_2 tuum/kest nanotraadi käitumist paindekatses elektronkiire kiirguse all. Võrreldes eksperimentaalset tulemust FEM-mudeliga, leiti, et isegi mõõduka voolu ja pingega elektroniir on võimeline tekitama muudatusi amorfses oksiidkestas.

Lõpuks võrreldi kahte Au nanotraatide kolme punkti paindekatse varianti: vabalt asetsevate ja libisevate otste ja jäigalt fikseeritud otste korral. Eksperimentaalselt määrati erinevate ääretingimuste mõju ja saadud tulemusi kasutati FEM-i modelleerimisel leidmaks Au ja aluse vahel olevaid adhesioonijõude.

Kokkuvõtvalt näidati, et FEM on võimas meetod nanoskaalas süsteemide mehaaniliste ja triboloogiliste omaduste uurimiseks, eriti kui seda kasutatakse kombinatsioonis koos eksperimentaalsete tulemustega.

6. ACKNOWLEDGMENTS

I would like to express gratitude to my supervisors Sergei Vlassov, Rünno Lõhmus and Leonid Dorogin for their support and guidance in my studies and research work in the Laboratory of Physics of Nanostructures, to all the coauthors and to the "Nanomanipulation Team" of our laboratory. This work was supported by the Estonian Science Foundation (grants JD162, IUT2-25) and also partly by COST Action MP1303. This work has been partially supported by Graduate School of Functional materials and technologies receiving funding from the European Regional Development Fund in University of Tartu, Estonia.

REFERENCES

[1] Weng, B.; Liu, S.; Tang, Z.-R. and Xu, Y.-J., RSC Adv., 2014, 4, , 12685
[2] Huang, Y; Bai, X. and Zhang, Y., J. Phys.: Condens. Matter 2006, 18, L179–L184
[3] García,E. J.; Hart, A. J.; and Wardle B.L.; AIAA JOURNAL, 2008, (46) 6,
[4] ONE-DIMENSIONAL NANOSTRUCTURES. Edited by TIANYOU ZHAI and JIANNIAN YAO. Hoboken, New Jersey, John Wiley & Sons, Inc., 2013.
[5] Dresselhaus, M. S.; Lin, Y.-M.; Rabin, O.; Black, M. R. and Dresselhaus, G., Springer Handbook of Nanotechnology, edited by Bharat Bhushan, 2004, pp. 99–145
[6] Wiley, B.; Sun, Y.; Xia, Y. Acc. Chem. Res., 2007, 40 (10), 1067– 1076
[7] Caswell, K. K.; Bender, C. M.; Murphy, C. J. Nano Lett., 2003, 3 (5), 667– 669
[8] Lee, P.; Lee, J.; Lee, H.; Yeo, J.; Hong, S.; Nam, K. H.; Lee, D.; Lee, S. S.; Ko, S. H. Adv. Mater., 2012, 24 (25), 3326– 3332
[9] Lee, J.; Lee, P.; Lee, H.; Lee, D.; Lee, S. S.; Ko, S. H. Nanoscale, 2012, 4, 6408–6414
[10] Barnes, W. L.; Dereux, A.; Ebbesen, T. W. Nature, 2003, 424, 824–830
[11] Wang, W.; Yang, Q.; Fan, F.; Xu, H.; Wang, Z. L. Nano Lett., 2011, 11 (4), 1603– 1608
[12] Wu B., Heidelberg A., Boland J. J., Sader J. E., Sun X., Li Y., Nano Lett. 2006, 6 (3), 468–72.
[13] Z. L. Wang, R. P. Gao, P. Poncharal, W. A. de Heer, Z. R. Dai and Z. W. Pan, Mater. Sci. Eng. 2001, C 16 3–10
[14] Ozbay, E. Science 2006, 311 (5758) 189– 193
[15] Engheta, N. Science, 2007, 317, (5845) 1698– 1702
[16] Schuh, C. H., Mater. Today, 9 (2006), pp. 32–40
[17] Minor, A. M.; Syed Asif, S. A.; Shan, Z.; Stach, E. A.; Cyrankowski, E.; Wyrobek, T. J. and Warren, O. L.; Nature Materials 2006 5, 697–702
[18] Saha, R.; Nix, W.D., Acta Mater., 2002, 50 (1), pp. 23–38
[19] Svintsov, A. A.; Trofimov, O. V. and Zaitsev, S. I., J. Vac. Sci. Technol. B 2007, 25, 6
[20] Gordon, M. J.; Baron, T.; Dhalluin, F.; Gentile, P.; Ferret, P., Nano Lett. 2009, 9, 525–529.
[21] Manoharan, M. P.; Desai, A. V.; Neely, G.; and Haque, M. A., J NANOMATER. 2008
[22] Zhang, H.; Tang, J.; Zhang, L; An, B. and Qin, L.-C., APPLIED PHYSICS LETTERS 2008, 92, 173121
[23] Corrales, T. P.; Friedemann, K.; Fuchs, R.; Roy, C.; Crespy, D. and Kappl, M., Langmuir 2016, 32, 1389–1395
[24] Xu, F.; Qin, Q.; Mishra, A.; Gu, Y. and Zhu, Y., Nano Res., 2010, 3 271–280.
[25] Yu, M. F.; Dyer, M. J.; Skidmore, G. D.; Rohrs, H. W.; Lu, X. K.; Ausman, K. D.; Ehr, J. R. V. and Ruoff, R. S., Nanotehcnology 1999, 10, 244–252.
[26] Zhang, Y., Dhaigude, M. and Wang, J., Procedia Manufacturing 2015, 1, 828–839
[27] 1]Mo, Y.; Turner K. T. and Szlufarska, I, *Nature* **457**, 1116–1119
[28] Roy, A., Xie, H., Wang, S. & Huang, H. Appl. Surf. Sci. 389, 797–801 2016.
[29] Qin Q, Zhu Y., ACS Nano. 2011 27;5(9):7404–10.
[30] Koskilinna, J.O.; Linnolahti, M.; Pakkanen, T.A., Tribol. Lett. 2006, 24(1), 37–41.

[31] Deshpande, V.S.; Needleman, A.; Van der Giessen, E.; Acta Mater. 2004, 52(10), 3135–3149.
[32] Hyun, S.; Pei, L.; Molinari, J.F. and Robbins, M.O., Phys. Rev. E 2004, 70(2), 026117.
[33] Wriggers, P.; Laursen, T.A., Computational Contact Mechanics (Springer, Dordrecht, 2008)
[34] Luan, B.; Robbins, M.O., Phys. Rev. E 2006, 74(2), 026111
[35] Mo, Y.; Szlufarska, I., Phys. Rev. B 2010, 81(3), 035405
[36] Spijker, P.; Anciaux, G.; Molinari, J.F., Comput. Mech. 2011, 50(3), 273–283.
[37] Rapaport, D.C. The Art of Molecular Dynamics Simulation (Cambridge University Press, 2004)
[38] Hughes, T.J.R. The Finite Element Method: Linear Static and Dynamic Finite Element Analysis (Dover Publications, New York, 2000)
[39] Zienkiewicz, O.C.; Taylor, R.L.; Zhu, J.Z., The Finite Element Method: Its Basis & Fundamentals (Elsevier Butterworth-Heinemann, Amsterdam, 2005)
[40] Berendsen, H.J.C., Simulating the Physical World: Hierarchical Modeling from Quantum Mechanics to Fluid Dynamics (Cambridge University Press, 2007)
[41] Griebel, M.; Knapek, S.; Zumbusch, G., Numerical Simulation in Molecular Dynamics: Numerics, Algorithms, Parallelization, Applications (Springer, November 2010)
[42] Yvonnet, J.; Mitrushchenkov, A.; Chambaud, G.; He, Q.-C., Comput. Methods Appl. Mech. Eng., 2011, 200, p. 614
[43] Leclere C. et al., J. Appl. Cryst. 2015, 48, 291–296
[44] Gong, R., Zhang, H., Che, H., Zhu, M., and Xu, Y., Int. J. Numer. Meth. Engng, 2016, 108: 1159–1173
[45] Jeng, Y.R., Su, C.-C.; Lay, Y.-T., Appl. Surf. Sci., 2007 253, 16, 6754–6761
[46] Xie, H. et al. Sci. Rep. 2017, 7, 44907
[47] Hembacher, S. et al, Appl. Surf. Sci. 2002, 188, 445–449.
[48] Seo, Y.; Cadden-Zimansky, P. and Chandrasekhar, V., Appl. Phys. Lett. 2005, 87, 103103
[49] Ng, B, P.; Zhang, Y.; Kok, S. W.; Soh, Y. C., Ultramicroscopy 2009, 109, 291–295.
[50] Huang M. H., Wu Y., Feick H., Tran N., Weber E., Yang P., Adv Mater 2001, 13, 113–6
[51] Gao P.X., Ding Y., Wang Z.L. ,Nano Lett 2003 9, 1315, 20.
[52] Dorogin L.M., Vlassov S., Polyakov B., Antsov M., Lõhmus R., Kink I., et al., Phys Status Solidi B 2012, 1–13.
[53] Zhu Z., Chen T.L., Gu Y., Warren J., Osgood R.M., Chem Mater 2005 17, 4227–34.
[54] Antsov, M.; Dorogin, L.; Vlassov, S.; Polyakov, B.; Vahtrus, M.; Mougin, K.; Lõhmus, R.; Kink, I. Tribology Int. 2014, 72, 31–34
[55] Yin, Y.; Lu, Y.; Sun, Y.; Xia, Y. Nano Lett. 2002, 2, 427–430
[56] Sioss, J. A.; Stoermer, R. L.; Sha, M. Y.; Keating, C. D. Langmuir 2007,23, 11334–11341.
[57] Vlassov, S.; Polyakov, B.; Dorogin, L. M.; Vahtrus, M.; Mets, M.;Antsov, M.; Saar R.; Romanov, A. E.; Löhmus, A.; Löhmus, R.Nano Lett. 2014, 14, 5201–5205
[58] Gao, C.; Lu, Z.; Yin, Y. Langmuir 2011, 27, 12201–12208.
[59] Silva, E. C. C. M.; Tong, L.; Yip, S.; van Vliet, K. J. Small 2006, 2 239–243.
[60] Vlassov, S.; Polyakov, B.; Dorogin, L. M.; Antsov, M.; Mets, M.;Umalas, M.; Saar, R.; Lõhmus, R.; Kink, I. Mater. Chem. Phys. 2014,143, 1026–1031.
[61] Van der Vegt, A. K. From Polymers to Plastics; VSSD: Delft, 2002.
[62] Afkhami S, Kondic L:, Phys Rev Lett 2013, 111,034501.

[63] Kondic L.; Diez J.A.:, Phys Rev E 2009, 79, 026302.
[64] Polyakov, B.; Vlassov, S.; Dorogin, L.; Novoselska, N.; Butikova, J.; Antsov, M.; Oras, S.; Lõhmus, R.; Kink, I.. Nanoscale Research Letters, 2014, 9.
[65] Bai X. D., Gao P. X., Wang Z. L. and Wang E. G. Appl. Phys. Lett. 2003, 82 4806–8
[66] Song, J.; Wang, X.; Riedo E.; Wang, Z. L., *Nano Lett.*, 2005, 5, 1954–1958.
[67] Desai A. V. and Haque M. A., Sensors Actuators A 2007,134 169–76
[68] Chen C.; Shi Y.; Zhang Y.; Zhu J. and Yan Y., Phys. Rev. Lett. 2006, 96 75505
[69] Wen B., Sader J. E. and Boland J. J., Phys. Rev. Lett. 2008, 101 2–5
[70] Stan G.; Ciobanu C. V.; Parthangal P. M. and Cook R. F. Nano Lett. 2007, 7 3691–7
[71] Manoharan M. P., Desai A. V., Neely G. and Haque M. A. J. Nanomater. 2008 1–7
[72] Ni H. and Li X. Nanotechnology 2006, 17 3591–7
[73] Ji L-W, Young S-J, Fang T-H and Liu C-H Appl. Phys. Lett. 2007, 90 033109
[74] Agrawal R.; Peng B,; Gdoutos E. E. and Espinosa H. D. Nano Lett. 2008, 8 3668–74
[75] Zhang L. and Huang H. Appl. Phys. Lett. 2006, 89 183111
[76] Polyakov, B.; Antsov, M.; Vlassov, S.; Dorogin, L. M.; Vahtrus, M.; Zabels, R.; Lange S.; Lõhmus, R. Beilstein J. Nanotechnol. 2014, 5, 1808–1814.
[77] Vlassov, S.; Polyakov, B.; Oras, S.; Vahtrus, M.; Antsov, M.; Šutka, A.; Smits, K.; Dorogin, L. and Lõhmus, R., Nanotechnology, 2016 27 (33), 335701.
[78] Handbook of Engineering Mechanics. Edited by W. FLÜGGE. New York: McGraw-Hill, 1962.
[79] Mets, M.; Antsov, M.; Zadin, V.; Dorogin, L.; Aabloo, A.; Polyakov, B.; Lõhmus, R. and Vlassov, S., Phys. Scr. 2016, 91, 115701 (7pp)
[80] Wang, J. et al. Nat. Commun. 2013, 4,1742 .
[81] Israelachvili J: Intermolecular and Surface Forces. London: Academic; 1992
[82] Ho C.Y., Taylor R.E., Thermal Expansion of Solids. Materials Park: ASM International; 1998
[83] Gao, C.; Lu, Z.; Yin, Y. *Langmuir* 2011**,** *27,* 12201–12208.
[84] Hertz, H. R. 1882, Ueber die Beruehrung elastischer Koerper (On The Contact Between Elastic Bodies). Gesammelte Werke (Collected Works); Leipzig, Germany, 1895; Vol. 1.

PUBLICATIONS

CURRICULUM VITAE

Name	Mikk Antsov
Date of birth	29.12.1987, Võhma, Estonia
Citizenship.	Estonia
Telephone	+37258164820
E-mail	+mikk.antsov@ut.ee

Current employment	University of Tartu, Institute of Physics, junior researcher
Education	
1996– 2004	Viljandi Paalalinna Secondary School, German language specialization
2004–2007	C. R. Jakobson Secondary School, mathematics-physics specialization
2007–2012	University of Tartu, Bachelor of Science (Physics)
2012–2013	University of Tartu, Master of Science (Physics)
2013–2017	University of Tartu, PhD studies in physics

Professional development

2014	"PhD Summer School in NanoTribology" (Technical University of Denmark)
2016	Short-term scientific mission to University of Giessen, Institute of Applied Physics, Germany

ELULOOKIRJELDUS

Nimi	Mikk Antsov
Sünniaeg	29.12.1987, Võhma, Eesti
Kodakondsus	Eesti
Telefon	+37258164820
E-mail	mikk.antsov@ut.ee
Praegune töökoht	Tartu Ülikool, Füüsika instituut, nooremteadur

Haridustee

1996–2004	Viljandi Paalalinna Gümnaasium, põhikool, saksa keele süvaõppe suund
2004–2007	C. R Jakobsoni nimeline Gümnaasium, matemaatika-füüsika eriklass
2007–2012	Tartu Ülikool, bakalaureuseõpe, füüsika eriala
2012–2013	Tartu Ülikool, magistriõpe, füüsika eriala
2013–2017	Tartu Ülikool, doktoriõpe, füüsika eriala

Erialane enesetäiendus

2014	Suvekool “NanoTriboloogias”, DTU, Taani Tehnika Ülikool
2016	Lühiajaline külalisteadlane Giesseni Ülikooli Rakendusfüüsika Instituudis Saksamaal

DISSERTATIONES PHYSICAE UNIVERSITATIS TARTUENSIS

1. **Andrus Ausmees.** XUV-induced electron emission and electron-phonon interaction in alkali halides. Tartu, 1991.
2. **Heiki Sõnajalg.** Shaping and recalling of light pulses by optical elements based on spectral hole burning. Tartu, 1991.
3. **Sergei Savihhin.** Ultrafast dynamics of F-centers and bound excitons from picosecond spectroscopy data. Tartu, 1991.
4. **Ergo Nõmmiste.** Leelishalogeniidide röntgenelektronemissioon kiiritamisel footonitega energiaga 70–140 eV. Tartu, 1991.
5. **Margus Rätsep.** Spectral gratings and their relaxation in some low-temperature impurity-doped glasses and crystals. Tartu, 1991.
6. **Tõnu Pullerits.** Primary energy transfer in photosynthesis. Model calculations. Tartu, 1991.
7. **Olev Saks.** Attoampri diapasoonis voolude mõõtmise füüsikalised alused. Tartu, 1991.
8. **Andres Virro.** AlGaAsSb/GaSb heterostructure injection lasers. Tartu, 1991.
9. **Hans Korge.** Investigation of negative point discharge in pure nitrogen at atmospheric pressure. Tartu, 1992.
10. **Jüri Maksimov.** Nonlinear generation of laser VUV radiation for high-resolution spectroscopy. Tartu, 1992.
11. **Mark Aizengendler.** Photostimulated transformation of aggregate defects and spectral hole burning in a neutron-irradiated sapphire. Tartu, 1992.
12. **Hele Siimon.** Atomic layer molecular beam epitaxy of A^2B^6 compounds described on the basis of kinetic equations model. Tartu, 1992.
13. **Tõnu Reinot.** The kinetics of polariton luminescence, energy transfer and relaxation in anthracene. Tartu, 1992.
14. **Toomas Rõõm.** Paramagnetic H^{2-} and F^+ centers in CaO crystals: spectra, relaxation and recombination luminescence. Tallinn, 1993.
15. **Erko Jalviste.** Laser spectroscopy of some jet-cooled organic molecules. Tartu, 1993.
16. **Alvo Aabloo.** Studies of crystalline celluloses using potential energy calculations. Tartu, 1994.
17. **Peeter Paris.** Initiation of corona pulses. Tartu, 1994.
18. **Павел Рубин.** Локальные дефектные состояния в CuO_2 плоскостях высокотемпературных сверхпроводников. Тарту, 1994.
19. **Olavi Ollikainen.** Applications of persistent spectral hole burning in ultrafast optical neural networks, time-resolved spectroscopy and holographic interferometry. Tartu, 1996.
20. **Ülo Mets.** Methodological aspects of fluorescence correlation spectroscopy. Tartu, 1996.
21. **Mikhail Danilkin.** Interaction of intrinsic and impurity defects in CaS:Eu luminophors. Tartu, 1997.

22. **Ирина Кудрявцева.** Создание и стабилизация дефектов в кристаллах KBr, KCl, RbCl при облучении ВУФ-радиацией. Тарту, 1997.
23. **Andres Osvet.** Photochromic properties of radiation-induced defects in diamond. Tartu, 1998.
24. **Jüri Örd.** Classical and quantum aspects of geodesic multiplication. Tartu, 1998.
25. **Priit Sarv.** High resolution solid-state NMR studies of zeolites. Tartu, 1998.
26. **Сергей Долгов.** Электронные возбуждения и дефектообразование в некоторых оксидах металлов. Тарту, 1998.
27. **Kaupo Kukli.** Atomic layer deposition of artificially structured dielectric materials. Tartu, 1999.
28. **Ivo Heinmaa.** Nuclear resonance studies of local structure in $RBa_2Cu_3O_{6+x}$ compounds. Tartu, 1999.
29. **Aleksander Shelkan.** Hole states in CuO_2 planes of high temperature superconducting materials. Tartu, 1999.
30. **Dmitri Nevedrov.** Nonlinear effects in quantum lattices. Tartu, 1999.
31. **Rein Ruus.** Collapse of 3d (4f) orbitals in 2p (3d) excited configurations and its effect on the x-ray and electron spectra. Tartu, 1999.
32. **Valter Zazubovich.** Local relaxation in incommensurate and glassy solids studied by Spectral Hole Burning. Tartu, 1999.
33. **Indrek Reimand.** Picosecond dynamics of optical excitations in GaAs and other excitonic systems. Tartu, 2000.
34. **Vladimir Babin.** Spectroscopy of exciton states in some halide macro- and nanocrystals. Tartu, 2001.
35. **Toomas Plank.** Positive corona at combined DC and AC voltage. Tartu, 2001.
36. **Kristjan Leiger.** Pressure-induced effects in inhomogeneous spectra of doped solids. Tartu, 2002.
37. **Helle Kaasik.** Nonperturbative theory of multiphonon vibrational relaxation and nonradiative transitions. Tartu, 2002.
38. **Tõnu Laas.** Propagation of waves in curved spacetimes. Tartu, 2002.
39. **Rünno Lõhmus.** Application of novel hybrid methods in SPM studies of nanostructural materials. Tartu, 2002.
40. **Kaido Reivelt.** Optical implementation of propagation-invariant pulsed free-space wave fields. Tartu, 2003.
41. **Heiki Kasemägi.** The effect of nanoparticle additives on lithium-ion mobility in a polymer electrolyte. Tartu, 2003.
42. **Villu Repän.** Low current mode of negative corona. Tartu, 2004.
43. **Алексей Котлов.** Оксианионные диэлектрические кристаллы: зонная структура и электронные возбуждения. Tartu, 2004.
44. **Jaak Talts.** Continuous non-invasive blood pressure measurement: comparative and methodological studies of the differential servo-oscillometric method. Tartu, 2004.
45. **Margus Saal.** Studies of pre-big bang and braneworld cosmology. Tartu, 2004.

46. **Eduard Gerškevitš.** Dose to bone marrow and leukaemia risk in external beam radiotherapy of prostate cancer. Tartu, 2005.
47. **Sergey Shchemelyov.** Sum-frequency generation and multiphoton ionization in xenon under excitation by conical laser beams. Tartu, 2006.
48. **Valter Kiisk.** Optical investigation of metal-oxide thin films. Tartu, 2006.
49. **Jaan Aarik.** Atomic layer deposition of titanium, zirconium and hafnium dioxides: growth mechanisms and properties of thin films. Tartu, 2007.
50. **Astrid Rekker.** Colored-noise-controlled anomalous transport and phase transitions in complex systems. Tartu, 2007.
51. **Andres Punning.** Electromechanical characterization of ionic polymer-metal composite sensing actuators. Tartu, 2007.
52. **Indrek Jõgi.** Conduction mechanisms in thin atomic layer deposited films containing TiO_2. Tartu, 2007.
53. **Aleksei Krasnikov.** Luminescence and defects creation processes in lead tungstate crystals. Tartu, 2007.
54. **Küllike Rägo.** Superconducting properties of MgB_2 in a scenario with intra- and interband pairing channels. Tartu, 2008.
55. **Els Heinsalu.** Normal and anomalously slow diffusion under external fields. Tartu, 2008.
56. **Kuno Kooser.** Soft x-ray induced radiative and nonradiative core-hole decay processes in thin films and solids. Tartu, 2008.
57. **Vadim Boltrushko.** Theory of vibronic transitions with strong nonlinear vibronic interaction in solids. Tartu, 2008.
58. **Andi Hektor.** Neutrino Physics beyond the Standard Model. Tartu, 2008.
59. **Raavo Josepson.** Photoinduced field-assisted electron emission into gases. Tartu, 2008.
60. **Martti Pärs.** Study of spontaneous and photoinduced processes in molecular solids using high-resolution optical spectroscopy. Tartu, 2008.
61. **Kristjan Kannike.** Implications of neutrino masses. Tartu, 2008.
62. **Vigen Issahhanjan.** Hole and interstitial centres in radiation-resistant MgO single crystals. Tartu, 2008.
63. **Veera Krasnenko.** Computational modeling of fluorescent proteins. Tartu, 2008.
64. **Mait Müntel.** Detection of doubly charged higgs boson in the CMS detector. Tartu, 2008.
65. **Kalle Kepler.** Optimisation of patient doses and image quality in diagnostic radiology. Tartu, 2009.
66. **Jüri Raud.** Study of negative glow and positive column regions of capillary HF discharge. Tartu, 2009.
67. **Sven Lange.** Spectroscopic and phase-stabilisation properties of pure and rare-earth ions activated ZrO_2 and HfO_2. Tartu, 2010.
68. **Aarne Kasikov.** Optical characterization of inhomogeneous thin films. Tartu, 2010.
69. **Heli Valtna-Lukner.** Superluminally propagating localized optical pulses. Tartu, 2010.

70. **Artjom Vargunin.** Stochastic and deterministic features of ordering in the systems with a phase transition. Tartu, 2010.
71. **Hannes Liivat.** Probing new physics in e+e− annihilations into heavy particles via spin orientation effects. Tartu, 2010.
72. **Tanel Mullari.** On the second order relativistic deviation equation and its applications. Tartu, 2010.
73. **Aleksandr Lissovski.** Pulsed high-pressure discharge in argon: spectroscopic diagnostics, modeling and development. Tartu, 2010.
74. **Aile Tamm.** Atomic layer deposition of high-permittivity insulators from cyclopentadienyl-based precursors. Tartu, 2010.
75. **Janek Uin.** Electrical separation for generating standard aerosols in a wide particle size range. Tartu, 2011.
76. **Svetlana Ganina.** Hajusandmetega ülesanded kui üks võimalus füüsikaõppe efektiivsuse tõstmiseks. Tartu, 2011
77. **Joel Kuusk.** Measurement of top-of-canopy spectral reflectance of forests for developing vegetation radiative transfer models. Tartu, 2011.
78. **Raul Rammula**. Atomic layer deposition of HfO_2 – nucleation, growth and structure development of thin films. Tartu, 2011.
79. **Сергей Наконечный.** Исследование электронно-дырочных и интерстициал-вакансионных процессов в монокристаллах MgO и LiF методами термоактивационной спектроскопии. Тарту, 2011.
80. **Niina Voropajeva.** Elementary excitations near the boundary of a strongly correlated crystal. Tartu, 2011.
81. **Martin Timusk.** Development and characterization of hybrid electro-optical materials. Tartu, 2012, 106 p.
82. **Merle Lust.** Assessment of dose components to Estonian population. Tartu, 2012, 84 p.
83. **Karl Kruusamäe.** Deformation-dependent electrode impedance of ionic electromechanically active polymers. Tartu, 2012, 128 p.
84. **Liis Rebane.** Measurement of the $W \to \tau\nu$ cross section and a search for a doubly charged Higgs boson decaying to τ-leptons with the CMS detector. Tartu, 2012, 156 p.
85. **Jevgeni Šablonin.** Processes of structural defect creation in pure and doped MgO and NaCl single crystals under condition of low or super high density of electronic excitations. Tartu, 2013, 145 p.
86. **Riho Vendt**. Combined method for establishment and dissemination of the international temperature scale. Tartu, 2013, 108 p.
87. **Peeter Piksarv.** Spatiotemporal characterization of diffractive and non-diffractive light pulses. Tartu, 2013, 156 p.
88. **Anna Šugai.** Creation of structural defects under superhigh-dense irradiation of wide-gap metal oxides. Tartu, 2013, 108 p.
89. **Ivar Kuusik.** Soft X-ray spectroscopy of insulators. Tartu, 2013, 113 p.
90. **Viktor Vabson**. Measurement uncertainty in Estonian Standard Laboratory for Mass. Tartu, 2013, 134 p.

91. **Kaupo Voormansik.** X-band synthetic aperture radar applications for environmental monitoring. Tartu, 2014, 117 p.
92. **Deivid Pugal.** hp-FEM model of IPMC deformation. Tartu, 2014, 143 p.
93. **Siim Pikker.** Modification in the emission and spectral shape of photo-stable fluorophores by nanometallic structures. Tartu, 2014, 98 p.
94. **Mihkel Pajusalu**. Localized Photosynthetic Excitons. Tartu, 2014, 183 p.
95. **Taavi Vaikjärv.** Consideration of non-adiabaticity of the Pseudo-Jahn-Teller effect: contribution of phonons. Tartu, 2014, 129 p.
96. **Martin Vilbaste.** Uncertainty sources and analysis methods in realizing SI units of air humidity in Estonia. Tartu, 2014, 111 p.
97. **Mihkel Rähn.** Experimental nanophotonics: single-photon sources- and nanofiber-related studies. Tartu, 2015, 107 p.
98. **Raul Laasner.** Excited state dynamics under high excitation densities in tungstates. Tartu, 2015, 125 p.
99. **Andris Slavinskis.** EST Cube-1 attitude determination. Tartu, 2015, 104 p.
100. **Karlis Zalite**. Radar Remote Sensing for Monitoring Forest Floods and Agricultural Grasslands. Tartu, 2016, 124 p.
101. **Kaarel Piip.** Development of LIBS for *in-situ* study of ITER relevant materials. Tartu, 2016, 93 p.
102. **Kadri Isakar.** ^{210}Pb in Estonian air: long term study of activity concentrations and origin of radioactive lead. Tartu, 2016, 107 p.
103. **Artur Tamm.** High entropy alloys: study of structural properties and irradiation response. Tartu, 2016, 115 p.
104. **Rasmus Talviste.** Atmospheric-pressure He plasma jet: effect of dielectric tube diameter. Tartu, 2016, 107 p.
105. **Andres Tiko.** Measurement of single top quark properties with the CMS detector. Tartu, 2016, 161 p.
106. **Aire Olesk.** Hemiboreal Forest Mapping with Interferometric Synthetic Aperture Radar. Tartu, 2016, 121 p.
107. **Fred Valk.** Nitrogen emission spectrum as a measure of electric field strength in low-temperature gas discharges. Tartu, 2016, 149 p.
108. **Manoop Chenchiliyan.** Nano-structural Constraints for the Picosecond Excitation Energy Migration and Trapping in Photosynthetic Membranes of Bacteria. Tartu, 2016, 115p.
109. **Lauri Kaldamäe.** Fermion mass and spin polarisation effects in top quark pair production and the decay of the higgs boson. Tartu, 2017, 104 p.
110. **Marek Oja.** Investigation of nano-size α- and transition alumina by means of VUV and cathodoluminescence spectroscopy. Tartu, 2017, 89 p.
111. **Viktoriia Levushkina**. Energy transfer processes in the solid solutions of complex oxides. Tartu, 2017, 101 p.